Astron. Astrophys. 364, 391–408 (2000)

ASTRONOMY AND ASTROPHYSICS

86 GHz VLBI survey of compact radio sources⋆

A.P. Lobanov[1], **T.P. Krichbaum**[1], **D.A. Graham**[1], **A. Witzel**[1], **A. Kraus**[1], **J.A. Zensus**[1,3], **S. Britzen**[1,4], **A. Greve**[2], **and M. Grewing**[2]

[1] Max-Planck-Institut für Radioastronomie, Auf dem Hügel 69, 53121 Bonn, Germany
[2] IRAM, Grenoble, 300 Rue de la Piscine, 38460 St. Martin d'Héres, France
[3] National Radio Astronomy Observatory, 520 Edgemont Rd., Charlottesville, VA 22903, USA
[4] Present address: JIVE, Postbus 2, Dwingeloo AA 2990, The Netherlands

Received 17 September 1999 / Accepted 12 October 2000

Abstract. We present results from 86 GHz VLBI[1] observations of 28 compact radio sources made in April 1993. All but two of the observed objects are active galactic nuclei. The remaining two objects are the galactic center Sgr A* and the X-ray binary star Cygnus X-3. Of the observed sources, 26 have yielded fringe detections. We present correlated flux densities, estimate the maximum observed brightness temperatures, and provide single Gaussian component model fits. Out of the 17 sources with good *uv*-coverages, 3 are without detectable structural details (0642+449, 0716+714, and Cygnus A), 3 have little closure phase information (4C67.05, 1823+568, and 1928+738), and the remaining 11 have been imaged. We study the brightness temperatures, $T_{\rm b}$, of the observed sources, and apply a basic population model with a single value of the intrinsic brightness temperature, T_0, in order to reproduce the observed distribution of $T_{\rm b}$. Our data are consistent with a population of sources that have $T_0 \leq 5 \times 10^{10}$ K in the jets, and $T_0 \sim 1$–4×10^{11} K in the VLBI cores. The observed $T_{\rm b}$ are also correlated with the apparent speeds measured in the jets. For comparison, we apply the same population scenario to a larger sample of 132 AGN observed with VLBI at 15 GHz, and show that the distribution of brightness temperatures from that sample is consistent with the intrinsic brightness temperature of $T_0 = 5.3 \times 10^{11}$ K. The observed decrease of $T_{\rm b}$ along the jets can be reproduced by adiabatic losses in relativistic shocks embedded in the jet.

Key words: galaxies: active – galaxies: jets – galaxies: nuclei – galaxies: quasars: general – radio continuum: galaxies

1. Introduction

VLBI continuum observations at 86 GHz (3.5 mm) have been made since 1988, and have enabled probing the most compact regions in active galactic nuclei (AGN). Several detection and imaging surveys have been undertaken, with the total number of detected sources nearing 100 (see Beasley et al. 1996; Lonsdale et al. 1998; and Rantakyrö et al. 1998). These observations have enabled studies of the morphology of the parsec-scale jets on sub-milliarcsecond scales, and revealed increased curvature (Rantakyrö et al. 1998) and significant misalignment (Lonsdale et al. 1998) of the jets on these scales, compared to the larger scale structures observed with VLBI at lower frequencies. Multiple epoch VLBI observations at 86 GHz have been made for several sources, including most notably 3C 111 (Doeleman & Claussen 1996), 3C 454.3, (Krichbaum et al. 1995, 1996), NRAO 530 (Bower et al. 1997). The intrinsic size and structure of the Galactic Center have been studied in several VLBI observations at 86 GHz (Krichbaum et al. 1994a; Krichbaum 1998; Doeleman et al. 1998).

In this paper, we present 86 GHz VLBI observations of 28 radio sources which constitute one of the two parts of a coordinated millimeter VLBI campaign in April 1993. Results from the other part of the campaign have been presented by Rantakyrö et al. (1998). The main aim of the observations was to determine the number of sources suitable for imaging with VLBI at 86 GHz. The observations were one of the first systematic studies of a large sample of radio sources with VLBI at 86 GHz, albeit limited by uncertainty of amplitude calibration and a small number of participating radio telescopes. Inclusion of larger radio telescopes in Europe has improved the sensitivity of the data from the April 1993 campaign by a factor of 3, compared to the observations of Beasley et al. (1996) and Lonsdale et al. (1998). For many of the observed objects, however, we could only obtain "snapshot" *uv*-coverages, which limits the dynamic range and structural sensitivity of the data.

Preliminary results from the survey have been presented by Krichbaum et al. (1994b, 1995, 1996), Schalinski et al. (1994), and Standke et al. (1994). For several of the observed sources, the presented data are first VLBI observations at 86 GHz. We describe the observations and post-processing in Sect. 2. Particular attention is paid to the discussion of the antenna gain calibration (described in Sect. 2.1) and procedures employed for analyzing the structure of the observed objects (Sect. 2.2). The results and

Send offprint requests to: A.P. Lobanov

⋆ Figs. 25 to 30 are only available in electronic form with the On-line publication at http://link.springer.de/linl/service/journals/00230/tocs/t0364002/. Tables 1,4,5 are also available at the CDS via anonymous ftp to cdsarc.u.strasbg.fr(130.79.128.5) or via http://cdsweb.u.strasbg.fr/cgi-bin/gcat?J/A+A/(vol)/(page).

[1] Very Long Baseline Interferometry

Table 1. Source list

Name		α_{2000} (1)	δ_{2000} (2)	Status (3)	$z^\dagger$ (4)	Type† (5)	$m_v^\dagger$ (6)	$T_{\rm b,max}$ (7)
0016+731		00 19 45.78675	+73 27 30.0189	$-$	1.781	LPQ	18.0	
0212+735		02 17 30.81339	+73 49 32.6233	$+\,L$	2.367	HPQ/BL	19.0	>0.6
0224+671	4C67.05	02 28 50.05172	+67 21 03.0310	$++$	...	...	...	>27
0235+164		02 38 38.93006	+16 36 59.2789	$+\,L$	0.940	BL Lac	19.0	>1
0420−014		04 23 15.80059	−01 20 33.0627	$-\,RL$	0.915	HPQ/BL	17.8	
0528+134		05 30 56.41665	+13 31 55.1484	$+\,L$	2.06	LPQ/BL	20.0	29
0552+398	DA193	05 55 30.80564	+39 48 49.1654	$+$	2.365	LPQ	18.0	4
0642+449		06 46 32.02621	+44 51 16.5903	$++$	3.396	LPQ	18.5	47
0716+714		07 21 53.44791	+71 20 36.3611	$++$	0.300	HPQ	15.5	2
0836+710	4C71.07	08 41 24.36799	+70 53 42.1770	$++\,L$	2.17	LPQ	16.5	3
0923+392	4C39.25	09 27 03.01375	+39 02 20.8505	$++\,L$	0.699	LPQ	17.9	3
1226+023	3C273B	12 29 06.69970	+02 03 08.5958	$+\,RL$	0.158	LPQ	12.9	50
1228+126	3C274	12 30 49.42358	+12 23 28.0440	$+\,L$	0.004	E/Sy	9.6	6
1253−055	3C279	12 56 11.16667	−05 47 21.5392	$++\,RL$	0.538	HPQ/BL	17.8	110
1641+399	3C345	16 42 58.80967	+39 48 36.9957	$++\,RL$	0.594	HPQ	16.0	15
1730−130	NRAO530	17 33 02.70566	−13 04 49.5442	$++$	0.902	LPQ/BL	18.5	15
1742−289	Sgr A*	17 45 40.08483	−29 00 27.7795	$+$	...	Sa/Sy	...	4
1749+096		17 51 32.81846	+09 39 00.7315	$++$	0.322	HPQ/BL	16.8	9
1803+784		18 00 45.68364	+78 28 04.0206	$++\,L$	0.680	BL Lac	17.0	1
1823+568		18 24 07.06809	+56 51 01.4939	$++\,L$	0.664	BL Lac	18.4	10
1928+738		19 27 48.49468	+73 58 01.5723	$++\,L$	0.302	LPQ	16.5	16
1957+405	Cygnus A	19 59 28.35839	+40 44 02.4249	$++$	0.056	E/Sy	15.5	14
2005+403		20 07 44.94499	+40 29 48.6113	$+$	1.736	LPQ	19.5	>0.5
2007+777		20 05 30.99883	+77 52 43.2493	$+$	0.342	BL Lac	16.5	>0.1
2030+407	Cygnus X-3	20 32 25.76740	+40 57 28.2794	$+$	...	Star	...	>1
2145+067	DA 562	21 48 05.45857	+06 57 38.6061	$++\,RL$	0.990	LPQ	16.5	17
2230+114	CTA102	22 32 36.40937	+11 43 50.9024	$++\,RL$	1.037	HPQ/BL	17.3	4
2251+158	3C454.3	22 53 57.74786	+16 08 53.5655	$++\,RL$	0.859	HPQ/BL	16.1	9

Notes: † – information obtained from NASA/IPAC Extragalactic Database, http://nedwww.ipac.caltech.edu. Column designation: 1,2 – source coordinates; 3 – status: "–" – not detected; "+" – detected; "++" – detected and imaged; "R" – observed by Rantakyrö et al. (1998); "L" – observed by Lonsdale et al. (1998); 4 – redshift; 5 – type; 6 – optical magnitude; 7 – highest brightness temperature (in units of 10^{10}K) measured from our data.

images obtained from the observations are presented in Sect. 3. In Sect. 4, we discuss the distribution of brightness temperatures measured in the observed sample of sources, and relate this distribution to the intrinsic brightness temperatures and apparent speeds in parsec-scale jets. We also provide a comparison between the brightness temperatures measured in our sample and those reported in the sample of radio sources monitored with the VLBA[2] at 15 GHz (Kellermann et al. 1998).

Throughout the paper, we use the positive definition of spectral index, α ($S \propto \nu^\alpha$), and assume a Hubble constant $H_0 = 100\,{\rm km\,s^{-1}Mpc^{-1}}$ and deceleration parameter $q_0 = 0.5$.

2. Observations

The observations presented in this paper were part of a coordinated millimeter VLBI campaign in April 1993. We have observed 28 objects: 26 AGN, the Galactic Center Sgr A*, and the X-ray binary star Cygnus X-3. The basic information about the observed objects is summarized in Table 1, including the references to other VLBI observations of these objects made at 86 GHz.

Fringes were detected on baselines between 5 participating telescopes (listed in Table 2). The data were recorded with a 112 MHz bandwidth, using the MK III VLBI system (Rogers et al. 1983) in mode A. The observations were made in left circular polarization (LCP). We recorded 3-4 scans per hour, using the time between VLBI scans for focus checks, pointing and calibration.

The data were correlated at the MK III VLBI correlator of the MPIfR[3], using a pre-integration time of 1 s. The data were subsequently fringe fitted, edited, and calibrated using the MPIfR correlator software (Alef 1989), the CalTech VLBI package (Pearson 1991), and Difmap software (Shepherd et al. 1994). To reduce the detection threshold, the scans with weaker detections were re-fringe fitted, using smaller search windows centered around rate and delay values extrapolated from adjacent scans with stronger detections (for details of the method, see Krichbaum et al. 1992). In order to confirm the weaker detections found, we applied also the new method of incoherent fringe

[2] Very Long Baseline Array, operated by National Radio Astronomy Observatory, USA

[3] Max-Planck-Institut für Radioastronomie, Bonn, Germany

search (programs AVERAGE and SEARCH) implemented in the HOPS-package (Rogers et al. 1995).

The procedure described above has yielded fringe detections for 26 objects. Fringes have not been found in the data for 0016+731 and 0420-014 (most likely due to poor weather conditions during the observations).

2.1. Amplitude calibration

The fringe fitted data were amplitude calibrated using regular measurements of the system temperatures and antenna temperatures. Where possible, time-dependent factors in the antenna power gains were accounted for by applying atmospheric opacity corrections. We have also made corrections for pointing errors of the Effelsberg antenna, applying total flux density measurements made during the observations, in the gaps between the VLBI scans.

In order to check the visibility amplitudes, we have compared, where possible, close uv-points from different baselines, attempting to solve for the antenna gains. As an additional check for the accuracy and consistency of the amplitude calibration, we have tested (independently for each of the detected sources) the calibrated visibility amplitudes against single Gaussian component models obtained from the data (the corresponding models are given in Table 4). For each of the sources, the antenna gains were allowed to be scaled by a constant factor so as to optimize the fit by the Gaussian model. In one set of the trials, variations of the antenna gains were unrestricted. In the second set of the trials, the antenna gains were assumed to have 20% errors. We then inspected the corrections obtained, searching for possible systematic offsets or singular cases of exceedingly large correction factors.

The obtained corrections are within 10% for most of the sources, which is also reflected in the average corrections factors listed in Table 3. On the average, the gain factors for Pico Veleta, Haystack, and Quabin remain essentially unchanged. The averaged gain changes for Effelsberg and Onsala suffer from the substantial corrections required by the trials for 4C39.25, 1823+568 and 3C454.3. The larger corrections obtained for 4C39.25, 3C454.3, and 1749+096 are most likely due to the presence of extended structures not accounted for by the single Gaussian component models, and therefore are not likely to indicate calibration errors. The only source in which we expect to have serious calibration errors is 1823+568. If we exclude 4C39.25, 1823+568, 3C454.3, the average corrections for both Effelsberg and Onsala fall within 5%. We therefore conclude that systematic gain errors are not likely to compromise our data. Time-dependent errors may still be present in the calibrated data, which results in overall expected calibration accuracy of 20–30%. The absence of larger calibration errors can also be inferred from Fig. 5 and Columns 6–10 of Table 4 which show that in all of the observed sources, the correlated flux densities are always smaller than the respective total flux density.

Table 2. Technical parameters of participating telescopes

Name	Code	D[a] [m]	Gain [K/Jy]	$T^b_{\rm sys}$ [K]	$\eta^c_{\rm A}$
Effelsberg	E	60[d]	0.13	350	0.13
Onsala	S	20	0.056	250	0.49
Pico Veleta	P	30	0.14	180	0.55
Quabbin	Q	14	0.024	320	0.43
Haystack	K	37	0.058	200	0.15

Notes: a – diameter; b – system temperature; c – efficiency; d – effective illuminated diameter at 86 GHz.

Table 3. Average antenna gain corrections

Telescope	Unrestriced corrections	Restricted corrections
Effelsberg (E)	1.170±0.288	1.155±0.362
Onsala (S)	0.819±0.144	0.897±0.128
Pico Veleta (P)	1.028±0.153	0.984±0.043
Haystack (K)	1.032±0.149	1.027±0.057
Quabbin (Q)	1.015±0.303	1.012±0.044

2.2. Structure analysis

The *uv*-data available for each of the observed sources is described in Table 4 (Columns 2–10) which lists the number of visibility and closure phase datapoints, the time span covered by observations, and the correlated flux densities measured on different baselines. The distributions of visibility amplitudes are presented in Appendix C for several objects in which the observations have enabled detailed analysis of compact structure. Because of the small number of baselines and visibility datapoints and relatively high uncertainties of the amplitude calibration, we have adopted a three-step procedure intended to minimize the possibility of introducing errors into the structural information derived from the survey data.

2.2.1. Single-component models

As the first step, we model the visibility data for each object by a single elliptical Gaussian component, and examine the agreement between the model and observed visibility amplitudes and (where available) closure phases. The resulting single-component modelfits are presented in Columns 11–14 of Table 4. For seven of the objects observed (0212+735, 0528+134, DA193, Sgr A*, 2005+403, 2007+777, and Cygnus X-3), a single-component model is the only kind of structural information that can be obtained from the survey data. For the other eight objects (0224+671, 0235+164, 0642+690, 0716+714, 3C274, 1823+568, 1928+738, and Cygnus A), imaging is possible, but the amount of data available is too small to localize reliably the extended structures. For all these objects (except 0224+671), we apply the single-component model fits as starting models and make images, comparing the noise level in the images with the RMS-noise for the Gaussian models. For 0224+671, a two-component model listed in Table 5 was used as a starting guess.

Table 4. Correlated fluxes, single Gaussian component modelfit parameters, and CLEAN image parameters of the survey sources

Source	Database Description				Total and Correlated Flux Densities					Modelfit Parameters				Image Parameters				
	Array	$N_{\rm uv}$	$N_{\rm clo}$	$N_{\rm s}$	$S_{\rm tot}$	S_B	B	S_B	B	S	a	b/a	ϕ	$S_{\rm t}$	$S_{\rm p}$	$S_{\rm n}$	σ	$Beam$
(1)	(2)	(3)	(4)	(5)	(6)	(7)	(8)	(9)	(10)	(11)	(12)	(13)	(14)	(15)	(16)	(17)	(18)	(19)
0212+735	EPK	76	...	2	1.4	0.2 ± 0.1	440	0.2 ± 0.1	1600	1.3	0.35	1.0	...					
0224+671	SPK	148	37	2	2.2	0.3 ± 0.1	700	0.2 ± 0.1	1600	0.5	0.13	0.3	162	0.33	0.16	3.5	1.8	$0.15; 0.06; -3$
0235+164	ESKQ	149	...	3	3.1	0.8 ± 0.3	20	0.5 ± 0.2	1400	0.8	0.32	0.2	3	0.92	0.61	6.9	2.2	$0.64; 0.08; 2$
0528+134	EK	114	...	3	5.1			0.5 ± 0.4	1500	4.1	0.11	0.6	69					
DA193	EPK	112	...	3	1.4			0.3 ± 0.1	1400	0.5	0.08	1.0	...					
0642+449	ESPK	185	...	4	1.1	0.4 ± 0.2	700	0.2 ± 0.1	1150	0.3	0.04	0.4	47	0.39	0.32	3.4	1.3	$0.21; 0.11; -61$
0716+714	ESPK	113	...	3	0.8	0.4 ± 0.2	430	0.2 ± 0.1	1550	0.4	0.06	1.0	...	0.36	0.30	5.2	1.7	$0.21; 0.08; 65$
0836+710	ESPK	181	62	4	1.1	0.4 ± 0.2	680	0.2 ± 0.1	1550	0.9	0.29	0.3	78	1.05	0.46	3.5	1.7	$0.24; 0.07; 78$
4C39.25	ESPKQ	299	74	4	5.4	0.3 ± 0.1	230	0.1 ± 0.1	1600	1.9	0.08	0.9	42	3.13	0.51	10.2	2.8	$0.15; 0.11; 19$
3C273B	EPK	226	75	3	20.1	12.0 ± 1.0	330	3.4 ± 0.1	1550	16.4	0.49	0.2	3	12.22	6.74	33.2	10.2	$0.28; 0.07; -2$
3C274	EPK	106	...	1	1.1	0.2 ± 0.1	380	0.2 ± 0.1	1600	0.3	0.03	1.0	...	0.32	0.32	6.0	2.0	$0.27; 0.06; 4$
3C279	EPK	111	36	2	13.0	3.1 ± 0.2	370	0.8 ± 0.1	1600	7.9	0.08	0.4	94	7.92	4.51	9.0	3.1	$0.38; 0.06; -1$
3C345	ESPK	300	74	2	6.3	0.8 ± 0.2	720	0.3 ± 0.1	1200	5.6	0.68	0.7	295	2.89	1.35	14.0	5.2	$0.18; 0.09; -32$
NRAO530	ESPK	1260	310	11	6.3	4.5 ± 0.3	80	1.0 ± 0.3	1600	4.6	0.06	0.8	8	4.67	2.45	73.0	28.3	$0.35; 0.07; -2$
Sgr A*	EP	114	...	3	2.1	1.0 ± 0.5	300			1.3	0.22	1.0	...					
1749+096	ESPK	1792	741	11	3.0	0.8 ± 0.2	200	0.4–0.8	1600	0.8	0.07	0.4	24	1.46	0.66	20.0	6.1	$0.22; 0.06; 3$
						0.5–1.0	540											
1803+784	ESPK	443	37	8	1.5	0.8 ± 0.2	490	0.2 ± 0.1	1600	1.0	0.14	0.6	70	0.63	0.25	6.4	2.3	$0.14; 0.07; -31$
1823+568	ESPK	298	73	2	2.8	1.3 ± 0.3	720	0.7 ± 0.1	1550	0.8	0.05	1.0	...	1.30	1.02	10.0	3.3	$0.15; 0.06; -23$
1928+738	ESPK	334	...	7	1.3	0.3 ± 0.1	360	0.2 ± 0.1	1600	0.3	0.05	1.0	...	0.30	0.22	4.0	1.2	$0.17; 0.08; 11$
Cygnus A	ESPQ	149	...	2	1.8	0.8 ± 0.2	460	0.6 ± 0.3	1600	0.8	0.03	1.0	...	0.81	0.73	21.0	11.5	$0.17; 0.06; -19$
2005+403	EP	38	...	1	1.3	0.2 ± 0.1	485			1.2	0.32	1.0	...					
2007+777	ESP	149	...	4	1.4	0.6 ± 0.2	470			1.1	0.50	1.0	...					
Cygnus X-3	SPK	74	...	2	0.2			0.2 ± 0.1	1450	0.2	0.05	1.0	...					
2145+067	ESPKQ	410	73	4	5.4	1.2 ± 0.2	355	0.3 ± 0.1	1600	1.2	0.10	0.1	172	1.26	0.60	12.0	3.9	$0.31; 0.08; 5$
CTA102	ESPK	699	37	8	1.5	0.5 ± 0.2	600	0.2 ± 0.1	1600	0.5	0.10	0.6	351	1.28	0.50	12.6	3.4	$0.21; 0.06; 3$
3C454.3	ESPKQ	1798	784	13	8.2	2.2 ± 0.2	15	0.1–1.0	1600	1.8	0.08	0.1	92	2.76	0.70	24.5	7.6	$0.18; 0.07; 5$
						0.5–2.0	480											

Note: names of the sources for which an image is presented in this paper are given in bold. Column designation: 2 – participating telescopes (see Table 2 for technical details); 3 – number of uv-datapoints; 4 – number of closure phase datapoints; 5 – number of 6.5-minute long observing scans; 6 – total flux density [Jy] (obtained from pointing and calibration scan measurements made at Effelsberg); 7,9 – correlated flux density [Jy] measured on baselines 8,10 [Mλ]; 11–14 – model fit by a single Gaussian component: 11 – flux [Jy], 12 – major axis [mas], 13 – axial ratio, 14 – position angle of the major axis [$^\circ$]; 15–19 – image parameters: 15 – total CLEAN flux density [Jy], 16 – peak flux density [Jy/beam], 17 – lowest positive contour in the image [mJy/beam], 18 – off-source RMS in the image [mJy/beam], 19 – restoring beam major axis, minor axis, P.A. of the major axis [mas,mas,$^\circ$].

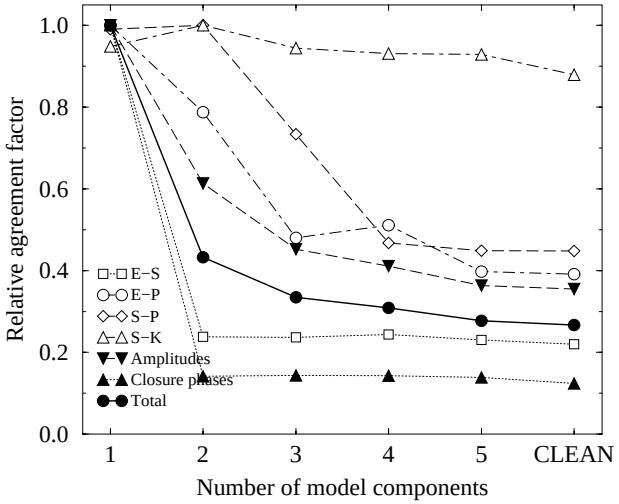

Fig. 1. 4C39.25. Model fit and CLEAN relative χ^2-agreement factors for the entire dataset (bold lines and filled symbols) and individual baselines (thin lines and open symbols). The agreement factors are normalized to their respective largest values.

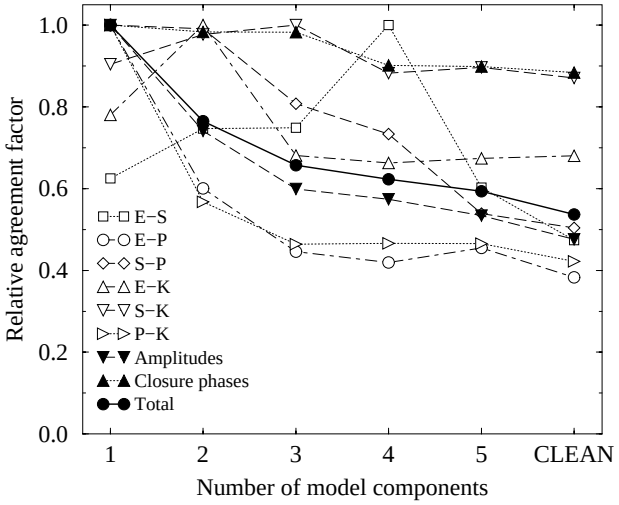

Fig. 2. 1749+096. Model fit and CLEAN relative χ^2-agreement factors for the entire dataset (bold lines and filled symbols) and individual baselines (thin lines and open symbols). The agreement factors are normalized to their respective largest values.

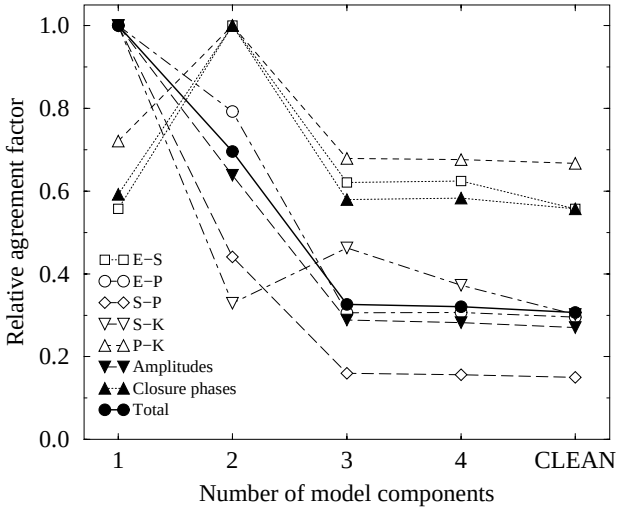

Fig. 3. 2145+067. Model fit and CLEAN relative χ^2-agreement factors for the entire dataset (bold lines and filled symbols) and individual baselines (thin lines and open symbols). The agreement factors are normalized to their respective largest values.

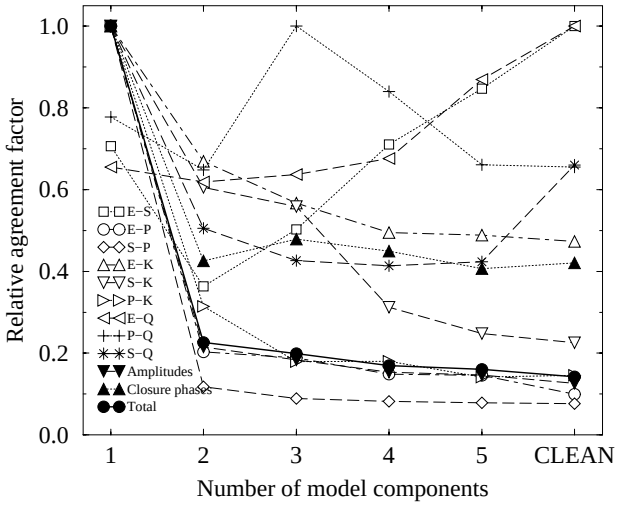

Fig. 4. 3C454.3. Model fit and CLEAN relative χ^2-agreement factors for the entire dataset (bold lines and filled symbols) and individual baselines (thin lines and open symbols). The agreement factors are normalized to their respective largest values.

The image parameters obtained are listed in Columns 15–19 of Table 4, for all objects which have been imaged.

2.2.2. Multi-component models

We obtain multi-component Gaussian models for the remaining 11 objects (printed in bold face in Table 4) in which the respective single-component model has a very small axial ratio or does not represent the data satisfactorily. The multi-component models contain 2–5 circular Gaussian components, depending on the complexity of the source structure. The complexity of the final multi-component model is determined for each of the modelled objects from monitoring of the changes of the agreement factors with increasing number of Gaussian components in the model. The modelling is stopped whenever the introduction of an additional Gaussian component does not lead to a sensible improvement of the fit (expressed quantitatively by the reduced χ^2-agreement factors). The resulting multi-component models and corresponding χ^2-agreement factors are presented in Table 5. Figs. 1–4 present relative changes of the χ^2-agreement factors depending on the number of the model components. The agreement factors are shown for the 4 objects in which more than 3 Gaussian components have been identified (4C39.25, 1749+096, 2145+067, and 3C454.3). For each object, we plot the agreement factors for the entire dataset, as well for individual baselines. All plotted quantities are normalized to their largest value. The x-axis gives the number of Gaussian components in

the respective models. For comparison, we also show the agreement achieved by the CLEAN δ-component model from the hybrid image of the respective source (see next section regarding the imaging procedure). Figs. 1–4 show convincingly the presence of extended structure in each of the presented objects: the agreement factors of multi-component models are 2–7 times better than the values obtained for the fits by single-component models.

2.2.3. Hybrid images

We produce hybrid maps of the 11 sources for which multi-component model fits have been made. For each object, its respective multi-component model is used as a starting guess. To improve image quality, we apply the self-calibration method (see Cornwell 1995) to the visibility phases. We do not modify visibility amplitudes, except for introducing an overall, time-constant gain correction factor wherever it is required for improving the agreement between the model and the data. Final images are produced using the CLEAN algorithm (Clark 1980) within tightly restricted areas. In several cases, we also produce images containing both elliptical Gaussian components and CLEAN δ-components.

The procedures described above have allowed us to control and verify the quality of the results at each of the step of the analysis, and we view them sufficient for establishing the reliability of the structural information we have obtained (within the limits determined by the quality of the data obtained for each of the observed objects).

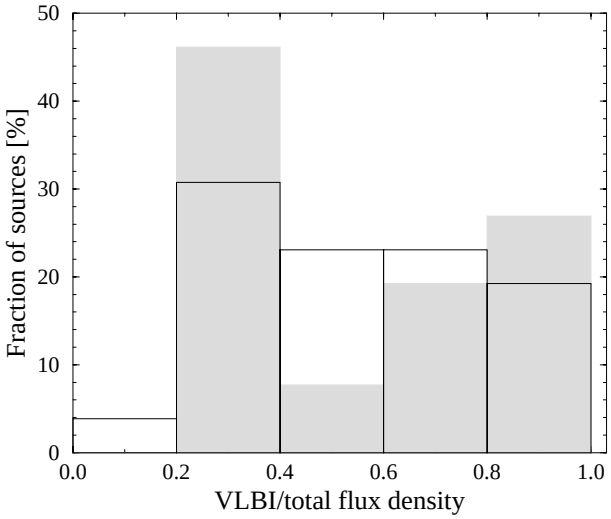

Fig. 5. Fractions of objects with given ratios of VLBI flux density to total flux density (Column 2 of Table 4). Open rectangles denote the ratio of the correlated flux densities on long baselines (Column 9 of Table 4) to the total flux densities. Filled rectangles show the ratio between the modelfit flux densities (Column 11 of Table 4) to the total flux densities. Both distributions indicate that roughly 75% of the observed sources are resolved at 86 GHz.

3. Results

For the detected sources, Table 4 lists the correlated flux densities measured on medium ($\leq 700\,\mathrm{M}\lambda$) and longest ($\geq 1200\,\mathrm{M}\lambda$) baselines. A single-component modelfit is also presented for each source in Table 4. For the sources with sufficient amount of data, formal image parameters are also listed (including the sources in which the available closure phase information precludes unambiguously locating the emission). The flux densities obtained from single component modelfits (Column 7 of Table 4) and the correlated flux densities measured on longest baselines (Column 5 of Table 4) both indicate that more than a half of the observed sources are resolved, and only one quarter remains unresolved (Fig. 5). We would like to emphasize that Fig. 5 reflects only the general properties of the *uv*-distributions observed, and does does not imply that the resolved objects may not contain a very compact and possibly unresolved core region.

3.1. Images and notes on individual sources

In Figs. 6–16 and Table 5, we present images and multi-component modelfits obtained for the sources with sufficient amount of data available. In all of the images, the contours are drawn at –1, 1, 1.5,...,1.5^n of the lowest flux density level, S_n, indicated in each individual image (and also listed in Table 4). For each image, Table 4 lists the total CLEAN flux, S_t, peak flux density, S_p, off-source RMS, σ, and parameters of the restoring CLEAN beam. For each of the imaged sources, the multi-component modelfits and corresponding brightness temperatures are given in Table 5. Circular Gaussians were used for all of the multi-component modelfits. Below, we discuss briefly the results for selected sources from our list. The same naming convention is adopted for all of the sources except 0224+671 and 4C39.25. We designate the "core" to be the most compact and bright component, and call it the component "C". Other detected components are called J1, J2, and so on, in decreasing order for increased separation from the core. In 0224+671, we are not able to distinguish the "core" component. For 4C39.25, we adopt the naming convention used by Alberdi et al. (1997).

0224+671

The *uv*-coverage obtained does not allow to locate unambiguously the position angle of the secondary component. We can only infer that the two components are separated by ∼0.1 mas. The model fit (see Table 5) gives $\theta = 26^\circ \pm 52^\circ$ for the position angle of the secondary component. This agrees roughly with the north-south elongation reported in the 1.4 GHz VLBI image of 0224+671 (Bondi et al. 1996). The inferred fluxes may, however, be too low, suffering from the lack of short baseline data.

0235+164

No closure phase information is available. The source appears to be resolved, as deduced from the measured correlated flux densities and the single component modelfit given in Table 4. At lower frequencies, the source is typically found to be unresolved (Kellermann et al. 1998; Gabuzda & Cawthorne 1996). At the epoch of the observation (1993.27), the 88 GHz light curve of the source has just passed through a maximum (Reuter et al. 1997),

Table 5. Multi-component modelfits

(1)	$S^a_{\rm peak}$ (2)	$S^b_{\rm tot}$ (3)	r^c (4)	θ^d (5)	d^e (6)	$T^g_{\rm b}$ (7)	$\chi^2_{\rm amp}$ (8)	$\chi^2_{\rm clo}$ (9)	$\chi^2_{\rm tot}$ (10)
				0224+671					
C1	158±16	159±23	...	...	0.01±0.01	16±4	0.93	1.53	1.26
C2	165±21	140±28	0.10±0.01	26±52	0.01±0.01	27±7	1.25	1.19	1.24
				0836+710					
C	461 ± 65	957 ± 149	...	...	0.12 ± 0.03	1.5 ± 0.5	1.98	1.50	1.85
J1	404 ± 45	566 ± 78	0.12 ± 0.02	199.0 ± 2.2	0.08 ± 0.02	3.2 ± 0.8	1.20	1.06	1.15
				4C39.25					
A	486 ± 73	630 ± 119	...	...	0.07 ± 0.02	3.0 ± 1.0	3.07	8.16	4.03
B	653 ± 115	1543 ± 362	0.24 ± 0.03	-40.9 ± 6.5	0.24 ± 0.06	0.2 ± 0.1	1.88	1.16	1.74
C1	144 ± 36	420 ± 75	0.78 ± 0.07	-66.2 ± 2.7	0.12 ± 0.03	0.4 ± 0.2	1.39	1.17	1.35
C2	66 ± 10	105 ± 18	1.82 ± 0.12	-75.2 ± 2.3	0.12 ± 0.04	0.2 ± 0.1	1.26	1.17	1.25
D	60 ± 10	116 ± 20	3.11 ± 0.18	-81.1 ± 2.1	0.04 ± 0.01	1.1 ± 0.4	1.12	1.13	1.12
				3C273B					
C	6750 ± 380	7880 ± 580	...	...	0.06 ± 0.03	50 ± 6	20.40	1.33	17.69
J1	6170 ± 470	4400 ± 580	0.05 ± 0.02	-90.9 ± 15.0	0.05 ± 0.02	46 ± 8	4.59	0.92	4.42
				3C279					
C	4510 ± 650	5050 ± 970	...	...	0.03 ± 0.01	110 ± 37	10.26	1.46	8.94
J1	2320 ± 290	2630 ± 450	0.07 ± 0.02	-81.1 ± 5.1	0.04 ± 0.02	36 ± 10	9.07	1.30	7.91
				3C345					
C	2070 ± 220	2610 ± 350	...	...	0.06 ± 0.04	15 ± 4	4.03	2.60	3.79
J1	655 ± 72	970 ± 130	0.17 ± 0.03	-62.9 ± 3.7	0.04 ± 0.02	11 ± 2.7	3.59	1.20	3.26
				NRAO530					
C	2450 ± 200	2380 ± 280	...	...	0.07 ± 0.03	15 ± 4	8.10	1.49	7.28
J1	1562 ± 150	1920 ± 244	0.27 ± 0.06	-0.9 ± 8.0	0.10 ± 0.03	5.1 ± 1.1	4.14	1.41	3.76
				1749+096					
C	708 ± 151	530 ± 188	...	...	0.04 ± 0.01	9.1 ± 4.3	2.38	1.32	2.12
J4	653 ± 115	451 ± 140	0.06 ± 0.10	-9.8 ± 6.9	0.08 ± 0.02	2.4 ± 0.9	1.76	1.30	1.62
J3	144 ± 36	156 ± 53	0.38 ± 0.04	0.2 ± 2.1	0.06 ± 0.02	0.8 ± 0.4	1.42	1.30	1.40
J2	142 ± 34	337 ± 86	1.31 ± 0.06	13.1 ± 6.2	0.12 ± 0.05	0.2 ± 0.1	1.36	1.19	1.32
J1	64 ± 20	65 ± 29	2.13 ± 0.08	22.2 ± 2.9	0.06 ± 0.04	0.4 ± 0.3	1.27	1.19	1.26
				1803+784					
C	254 ± 31	448 ± 63	...	...	0.08 ± 0.03	1.2 ± 0.3	1.38	1.91	1.42
J1	221 ± 28	376 ± 56	0.27 ± 0.06	-0.9 ± 8.0	0.08 ± 0.03	0.8 ± 0.2	1.07	1.88	1.15
				2145+067					
C	600 ± 89	647 ± 125	...	...	0.03 ± 0.01	17 ± 6	7.24	1.78	6.20
J3	327 ± 75	439 ± 126	0.09 ± 0.02	106.2 ± 4.0	0.06 ± 0.01	3.2 ± 1.6	4.62	3.00	4.31
J2	268 ± 61	431 ± 115	0.29 ± 0.06	107.0 ± 1.9	0.08 ± 0.02	1.2 ± 0.6	2.09	1.74	2.02
J1	31 ± 11	53 ± 22	0.46 ± 0.06	105.0 ± 0.9	0.03 ± 0.02	1.0 ± 0.8	2.05	1.75	1.98
				CTA102					
C	503 ± 67	638 ± 108	...	...	0.07 ± 0.02	3.5 ± 1.0	2.24	1.35	2.13
J2	150 ± 30	213 ± 525	0.08 ± 0.02	92.1 ± 5.8	0.08 ± 0.02	0.7 ± 0.3	2.02	1.38	1.96
J1	224 ± 40	464 ± 92	0.18 ± 0.07	157.0 ± 4.1	0.14 ± 0.04	0.4 ± 0.2	1.99	1.32	1.90
				3C454.3					
C	700 ± 92	866 ± 146	...	...	0.05 ± 0.01	8.7 ± 2.5	23.35	3.47	17.82
J4	142 ± 20	266 ± 42	0.22 ± 0.02	-28.8 ± 1.7	0.09 ± 0.02	0.5 ± 0.2	5.01	1.48	4.03
J3	747 ± 98	1076 ± 171	0.36 ± 0.03	-60.9 ± 0.7	0.07 ± 0.02	4.6 ± 1.3	4.28	1.66	3.55
J2	265 ± 37	313 ± 57	0.97 ± 0.10	-81.4 ± 0.7	0.05 ± 0.02	2.9 ± 0.9	3.59	1.56	3.02
J1	76 ± 19	125 ± 37	1.46 ± 0.11	-78.6 ± 1.0	0.20 ± 0.05	0.05 ± 0.03	2.94	1.46	2.53

Column designation: 1 – component name; 2 – peak brightness of the component measured in the image) [mJy/beam]; 3 – modelfit flux density of the component [mJy]; 4 – radius [mas]; 5 – position angle [°]; 6 – size [mas]; 7 – measured brightness temperature [$\times 10^{10}$K]; 8–10 – χ^2 of the fit after introducing the respective component into the model (top-to-bottom, beginning from the core); 8 – amplitude; 9 – closure phase; 10 – combined χ^2.

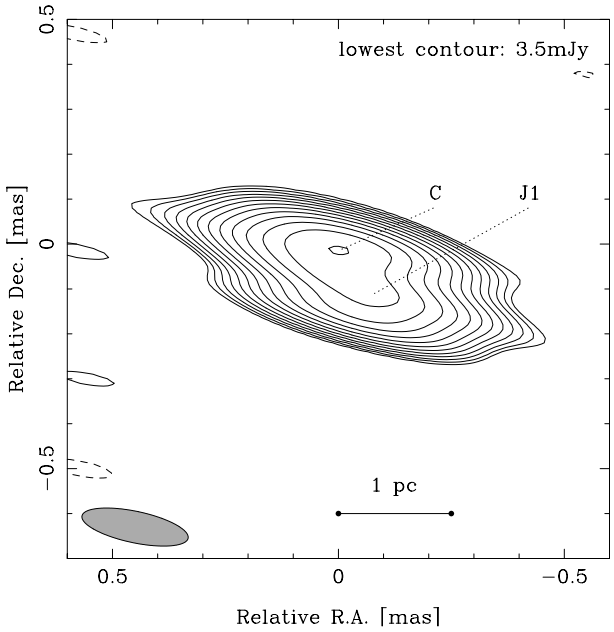

Fig. 6. Image of 0836+710. The image parameters are given in Table 4. Parameters of the components identified in the jet are given in Table 5. Shaded ellipse represents the FWHM of the restoring beam in the image.

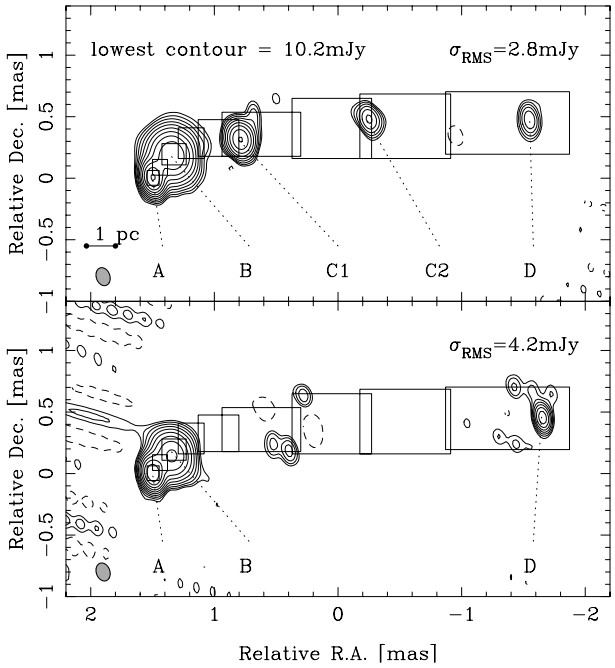

Fig. 7. Images of 4C39.25 based on a 5-component (top) and 3-component (bottom) Gaussian models of the source structure. The parameters of the image in the top panel are given in Table 4. Shaded ellipses represent the FWHM of the restoring beams. The locations of the Gaussian components are marked in each image. Parameters of the components identified in the top image are given in Table 5. Both images are produced in a similar way: the visibility phases have been calibrated with the respective Gaussian model, and 200 iterations of the CLEAN algorithm have been applied within a set of windows surrounding the Gaussian components. The sets of windows, shown in each panel, are identical for both images. In the bottom image, the off-source RMS noise is ∼30% higher, and there appears to be missing flux between the components B and D. The top image accounts for this flux.

the latter possibly indicating the ejection of a new plasmon into the jet, which would agree well with the observed extension of the source.

0642+449 and 0716+714

Both sources are resolved, and each is observed during a rise of its total flux at 88 GHz (Reuter et al. 1997). However, both sources appear essentially without structure, probably because of the insufficient *uv*-coverages.

0836+710

We have reanalyzed the data for 0836+710, and improved the original image presented by Krichbaum et al. (1996). The new image is shown in Fig. 6. A secondary component "J1" is seen at ≈0.1 mas separation from the core "C". The position angle of J1 is poorly constrained by our data. J1 can be identified with the jet feature B3 studied by Otterbein et al. (1998), who have related this feature to a broad-band flare which occurred in ∼1992.1 (von Linde et al. 1993). The further evolution of B3 can be explained by Kelvin-Helmholtz instabilities developing in the parsec-scale jet of 0836+710 (Lobanov et al. 1998).

4C39.25

The modelfit agreement factors are presented in Fig. 1. The image of 4C39.25 shown in the top panel of Fig. 7 reveals a bent jet outlined by 5 enhanced emission regions. We are able to locate these regions by model fitting the visibility data and applying the CLEAN algorithm to small areas tightly embracing the locations of the model fit components. The model fit components are presented in Table 5. The observation was originally presented by Alberdi et al. (1997), who fitted a model with 3 Gaussian components ("A", "B", and "D") to the visibility data, and compared the model with images of 4C39.25 made at lower frequencies. We have reanalyzed the data, and found evidence for emission between the components "B" and "D". This emission is also present in the images at 43 GHz. We represent this emission by two additional components ("C1" and "C2", in the notation of Alberdi et al. 1997).

In Fig. 7, we compare our 5-component model with the original 3-component model of Alberdi et al. (1997). Both images shown in Fig. 7 are produced using the same procedure: we first calibrate the phases with the Gaussian model, and then apply the CLEAN algorithm inside the windows shown in Fig. 7. The image obtained with the 3-component model has a higher noise level, and shows evidence for additional flux between the components B and D. The image obtained with our 5-component model accounts well for the flux between B and D, and has the RMS noise reduced by ∼30%.

Alberdi et al. (1997) identify the component D as the core of the jet, and argue that the increased brightness of the components A and B is caused by Doppler boosting. In our image (Fig. 7), the component A has the highest brightness temperature $T_{\rm b,A} = 3\times$

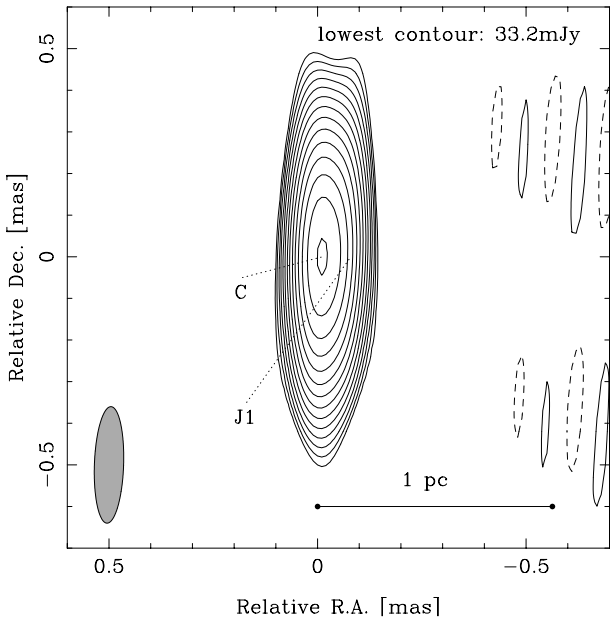

Fig. 8. Image of 3C273B. The image parameters are given in Table 4. Parameters of the components identified in the jet are given in Table 5. Shaded ellipse represents the FWHM of the restoring beam in the image.

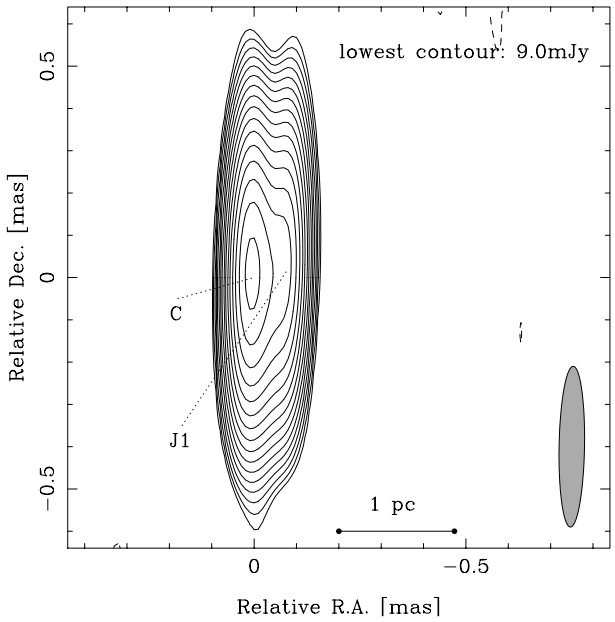

Fig. 9. Image of 3C279. The image parameters are given in Table 4. Parameters of the components identified in the jet are given in Table 5. Shaded ellipse represents the FWHM of the restoring beam in the image.

10^{10}K. The measured brightness temperature of the component D is lower: $T_{\rm b,D} = 1.1 \times 10^{10}$ K.

3C273B

In the image in Fig. 8, the secondary component J1 is poorly constrained by the data. 3C273 was observed nearly at the peak of a flare reaching in April 1993 a flux density of ≈28 Jy at 88 GHz (Reuter et al. 1997). Both the core C and the component J1 have a very high brightness temperature of $\sim 5 \times 10^{11}$ K. The component J1 can be identified with the feature C13 observed at later epochs at 43 and 86 GHz (Krichbaum et al. 1996).

3C274

Our data do not allow to detect any structure in the source. The single component modelfit given in Table 4 should be taken with caution.

3C279

For 3C279, we have reanalyzed the data, originally presented in Krichbaum et al. (1996). The source was observed nearly at the peak of a strong flare. In the image shown in Fig. 9, we are able to identify a secondary component located at a distance of ∼0.07 mas from the core. The *uv*-coverage is insufficient for imaging structures larger than ∼0.3 mas. Our data consist essentially of two adjacent scans, and the structural sensitivity of the dataset is obviously very poor. After a very careful examination of the calibration for 3C279 and several thorough cross-checks of the procedures applied, we are convinced that the observed extension is real. We have chosen a two-component representation for modelling this extension, in order to keep the consistency of all of the models produced. In the case of 3C279, a single-component modelfit cannot be made satisfactory unless a significant ellipticity is allowed for (see the respective numbers in Columns 11–14 of Table 4). Therefore, we resorted to introducing a second component into the model while preserving, in both components, the axial ratio of unity. Rantakyrö et al. (1998) also observed 3C279 in April 1993, during the same observing session of the CMVA. Their images show a more extended structure (owing to a better *uv*-coverage on short baselines), but lacks the resolution of our image.

3C345

The image in Fig. 10 shows clearly a double structure, with the jet component J1 separated by ∼0.2 mas from the core. J1 is most likely the result of the preceding flare which occurred in 1991 (Lobanov & Zensus 1999). This component can be associated with the jet component C8 detected at later epochs at lower frequencies (Ros et al. 1999; Leppänen et al. 1995).

NRAO530

The distribution of the visibility amplitudes is presented in Fig. 25 of Appendix C. The image in Fig. 11 shows a northward extension, with a secondary component J1 separated by ∼0.3 mas from the core. The position angle of the secondary component is poorly constrained by the data. We expect that $\theta_{\rm J1}$ is in the range of $\pm 10^{\circ}$. We are not able to find a satisfactory model with the source structure extended along $\theta \sim -90^{\circ}$ reported at the epoch of 1995.3 at 86 GHz (Bower et al. 1997). We find this apparent discrepancy acceptable, since substantial structural changes have been previously reported in NRAO530, with the position angle of extended emission varying between $\sim 0^{\circ}$ and $\sim -180^{\circ}$ (Marscher & Broderick 1981; Bondi et al. 1996). We do not detect the low brightness halo inferred from 86 GHz VLBI observations made in 1994.3 (Doeleman 1995) and 1995.3 (Bower et al. 1997). Our estimated brightness temperature of the core $T_{\rm b} \sim 1.5 \times 10^{11}$ K agrees well with the value $T_{\rm b} = (2.2 \pm 2.5) \times 10^{11}$ K obtained by Bower et al. (1997).

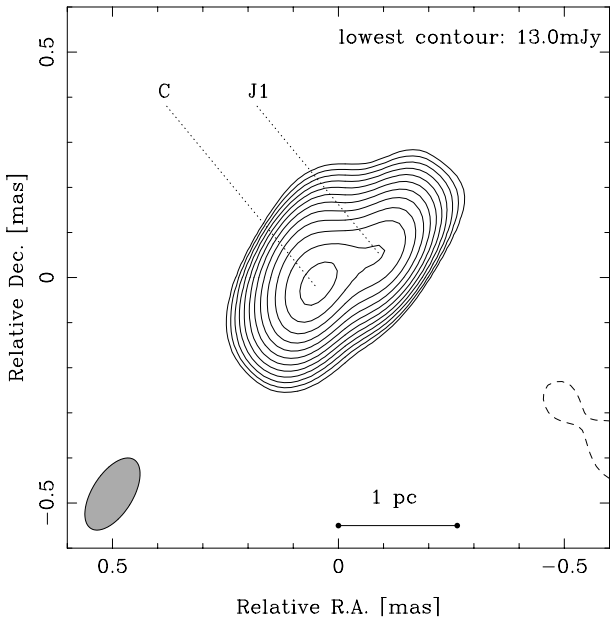

Fig. 10. Image of 3C345. The image parameters are given in Table 4. Parameters of the components identified in the jet are given in Table 5. Shaded ellipse represents the FWHM of the restoring beam in the image.

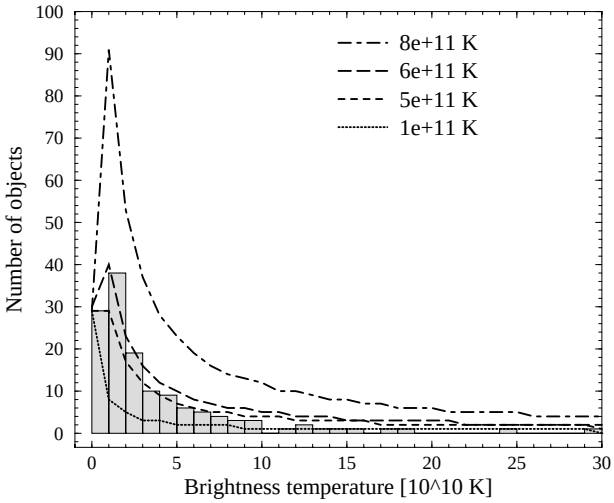

Fig. 11. Image of NRAO530. The image parameters are given in Table 4. Parameters of the components identified in the jet are given in Table 5. Shaded ellipse represents the FWHM of the restoring beam in the image.

Recent space VLBI observations made at 5 GHz indicate an even higher brightness temperature of the core in NRAO530 ($T_{\rm b} \sim 3 \times 10^{12}$ K, Bower & Backer 1998).

1749+096

The distribution of the visibility amplitudes is presented in Fig. 26 of Appendix C, and the modelfit agreement factors are shown in Fig. 2. The obtained *uv*-coverage allows imaging of fairly extended structures in the jet (Fig. 12). Conservative model fitting yields 4 components in the jet, with indications of additional, however ill-constrained, emission on larger scales.

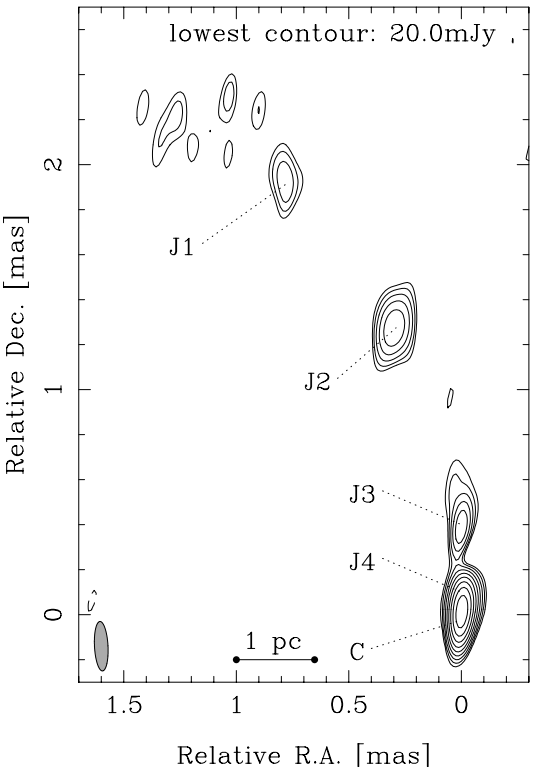

Fig. 12. Image of 1749+096. The image parameters are given in Table 4. Parameters of the components identified in the jet are given in Table 5. Shaded ellipse represents the FWHM of the restoring beam in the image.

At about 2 mas distance from the core, the jet appears to turn to P.A.$\sim 25^{\circ}$, which agrees well with the observations at lower frequencies (Gabuzda et al. 1996; Kellermann et al. 1998).

1803+784

A preliminary image was presented by Krichbaum et al. (1994b). The image in Fig. 13 shows a secondary component, J1, located to the West of the brighter core. We also detect traces of fainter emission farther away from the core, but are not able to constrain unambiguously its location, owing to insufficient *uv*-coverage of our data. Similar eastward extension of the jet is observed at lower frequencies (Kellermann et al. 1998). Our estimate of the brightness temperature of the core is smaller than that derived from VLBI observations at 8.4 GHz ($T_{\rm b} \approx 1.3 \times 10^{11}$K, Airapetyan & Matveenko 1997).

1823+568

Appears to be unresolved. The data, however, may have been affected by substantial calibration errors (see Sect. 2.1).

1928+738

No closure phases are available. The visibility distribution and the results from model fitting indicate that the source is resolved and has a size of about 0.05 mas.

Cygnus A

The *uv*-coverage is not sufficient for imaging the source. Model fitting gives a size of 0.03 mas, and a brightness temperature of $T_{\rm b} = (1.4 \pm 0.4) \times 10^{11}$K.

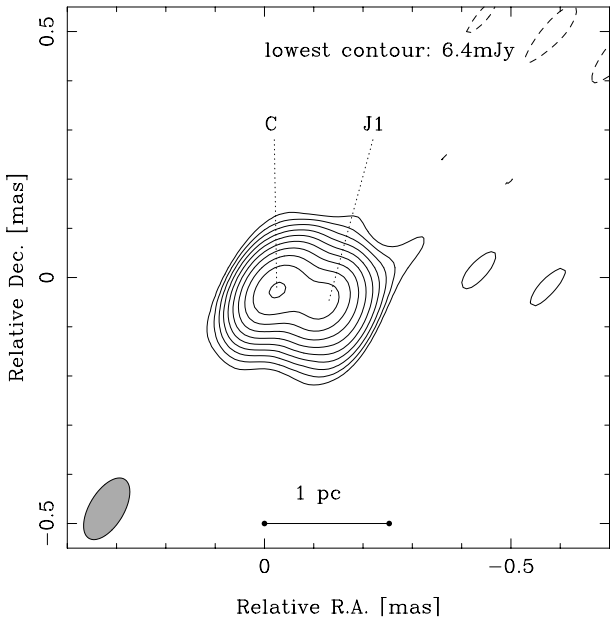

Fig. 13. Image of 1803+784. The image parameters are given in Table 4. Parameters of the components identified in the jet are given in Table 5. Shaded ellipse represents the FWHM of the restoring beam in the image.

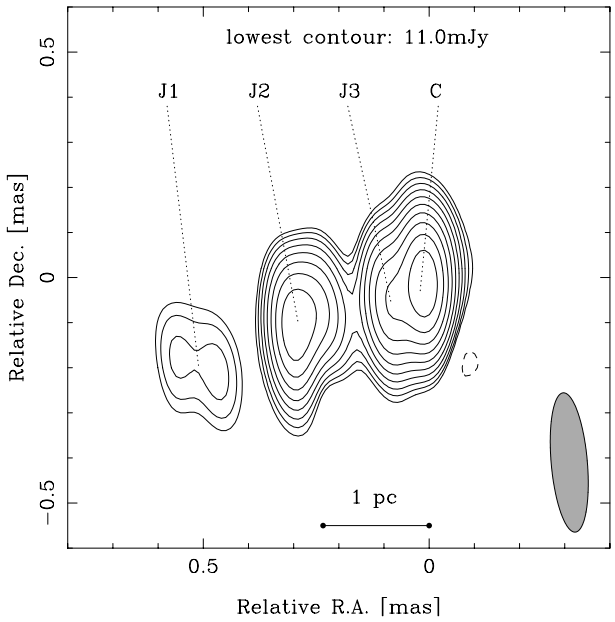

Fig. 14. Image of 2145+067. The image parameters are given in Table 4. Parameters of the components identified in the jet are given in Table 5. Shaded ellipse represents the FWHM of the restoring beam in the image.

2145+067

The distribution of the visibility amplitudes is presented in Figs. 27–28 of Appendix C, and the modelfit agreement factors are shown in Fig. 3. In the image in Fig. 14, we identify three features in the jet which extends along the P.A.$\sim 110^{\circ}$. Our results are substantially different from the conclusions of Rantakyrö et al. (1998), who do not detect extended structures in their 86 GHz observation made at the same epoch. The agreement factors listed in Table 5 strongly suggest the presence of at least two features in the jet, apart from the VLBI core "D". The extension of the jet along the P.A.$\approx$ 110 is supported by the projected visibility distribution plotted in Fig. 28. The position angle of the jet in our image in Fig. 14 is similar to that observed in VLBI images made at 15 GHz (Kellermann et al. 1998), 8.4 GHz (Airapetyan & Matveenko 1997), and 43 GHz (Lister, priv. comm.). The outermost feature in the jet (J1) is poorly constrained by the data. Our estimated brightness temperature of the core is about 5 times lower than that reported by Airapetyan & Matveenko (1997).

CTA102

The visibility amplitude distribution of the data is presented in Fig. 29 of Appendix C. The image in Fig. 15 shows a bent jet in which we are able to identify two emitting components. The direction of the jet is in a good agreement with VLBI images of CTA102 obtained at 22 GHz (Rantakyrö et al. 1996) and 15 GHz (Kellermann et al. 1998).

3C454.3

The distribution of the visibility amplitudes is presented in Fig. 30 of Appendix C, and the modelfit agreement factors are shown in Fig. 4. The data for 3C454.3 have been reanalyzed; the original image was presented by Krichbaum et al. (1995, 1996).

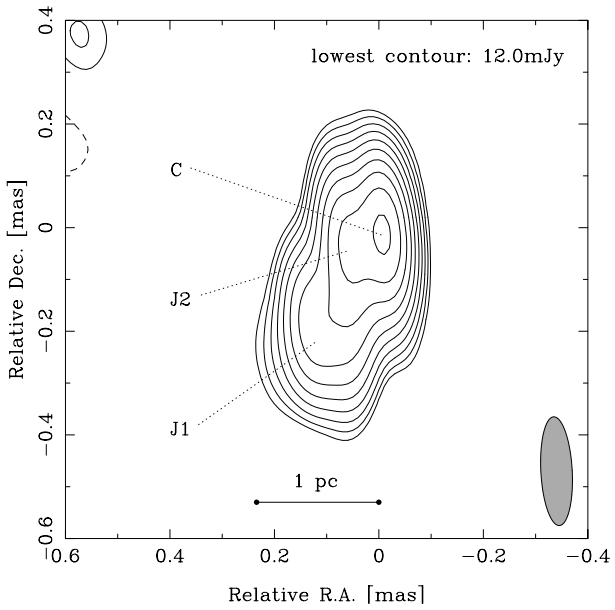

Fig. 15. Image of CTA102. The image parameters are given in Table 4. Parameters of the components identified in the jet are given in Table 5. Shaded ellipse represents the FWHM of the restoring beam in the image.

We have improved the image by calibrating the visibility phases by a model consisting of 5 circular Gaussians, and applying the CLEAN algorithm within small areas surrounding each of the model components. The resulting image is shown in Fig. 16.

*Sgr A**

The results of this single-baseline detection have been reported by Krichbaum et al. (1994a). Our reanalysis of the data

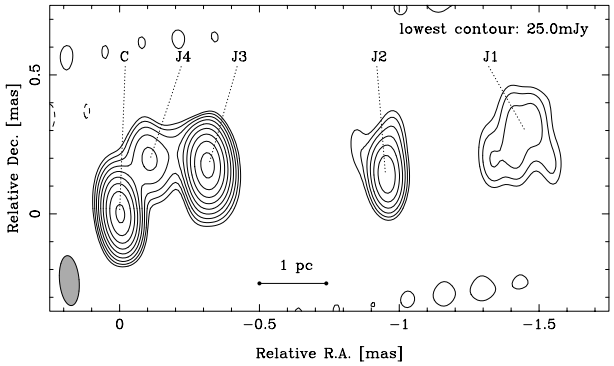

Fig. 16. Image of 3C454.3. The image parameters are given in Table 4. Parameters of the components identified in the jet are given in Table 5. Shaded ellipse represents the FWHM of the restoring beam in the image.

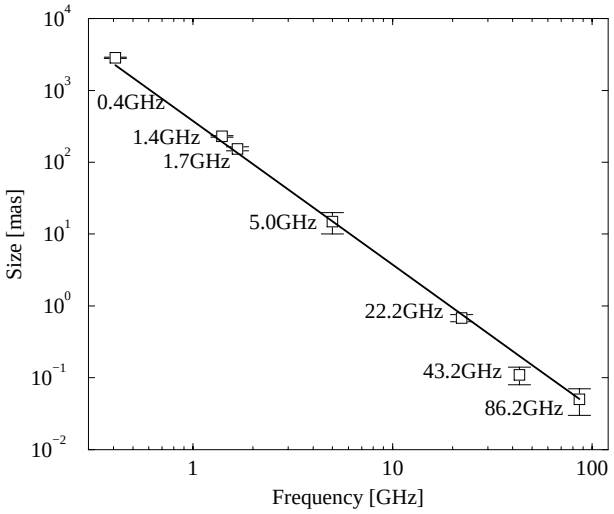

Fig. 17. Measured size of Cygnus X-3 at different frequencies. The measurements at 0.4–43.2 GHz are provided by Krichbaum & Schalinski (unpublished data). The datapoint at 86.2 GHz is from this paper. Solid line represents the scattering law (size $\propto \nu^{-2}$), indicating that Cygnus X-3 remains scattered even at 86 GHz.

yields a slightly weaker ($S = 1.3 \pm 0.4$ Jy), more compact ($d = 0.22 \pm 0.5$ mas) Gaussian component, corresponding to a slightly higher brightness temperature $T_{\rm b} = 4 \pm 2 \times 10^9$K. The derived size is in better agreement with the values obtained by Rogers et al. (1994) and Krichbaum et al. (1998).

Cygnus X-3

Cygnus X-3 is a well known X-ray binary with strongly variable radio emission, possibly originating from a relativistic outflow (Newell et al. 1998). Our data for Cygnus X-3 consist of weak detections on two long baselines of almost equal length ($\sim$ 1500 Mλ). The correlated flux measured on both baselines is close to the total flux (see Table 4). We fit a circular Gaussian to the visibility data, and obtain a formal estimate of 0.05 ± 0.02 mas for the size of the object. The radio emission from Cygnus X-3 is strongly scattered, and the obtained size indicates that at 86 GHz scattering is still present (see Fig. 17).

4. Brightness temperature and jet physics

Despite the sparse *uv*-coverages at 86 GHz, the brightness temperatures measured in our VLBI images provide a useful base for studying the general properties of compact jets. We combine the measured brightness temperatures, and apply a basic model of brightness temperature distribution, in order to deduce the collective properties of the 24 AGN observed. The range of conclusions that can be drawn from such a study is, however, limited, since a substantial fraction of the measured values are, in fact, lower limits of brightness temperature (Sect. 4.2).

4.1. Population model for the jet brightness temperatures

We model the distribution of the measured brightness temperatures by a simple population model based on the following assumptions:

a) all jets have the same Lorentz factor ($\gamma_{\rm j} = 10$ in our calculations, but the results depend weakly on the choice of this factor);

b) all jets have the same spectral index $\alpha = -0.7$, and the intrinsic brightness temperature, T_0, is the same for all jets;

c) the jets are assumed to be straight within the spatial scales ($\sim$0.5–10 pc) probed by the observations;

d) the jets are oriented randomly (within the limits of viewing angles required by Doppler boosting bias), and the observed distribution of measured brightness temperatures, $T_{\rm b}$, is caused solely by relativistic boosting of the emission.

For each measured $T_{\rm b}$, the corresponding Doppler factor is

$$\delta = (T_{\rm b}/T_0)^{\epsilon} \,. \qquad (1)$$

The power index ϵ is $1/(2-\alpha)$ for a continuous jet, and $1/(3-\alpha)$ for a single emitting plasmon (Blandford & Königl 1979).

For such a population of radio sources, one can readily see that the probability to find a radio source with the brightness temperature $T_{\rm b}$ is $\propto (2\gamma_{\rm j}\delta^{-1} - \delta^{-2} - 1)^{1/2}$ (see Appendix A for details of the derivation). If (as one may expect) the Lorentz factors, intrinsic brightness temperatures, and spectral indices vary in the jets, the corresponding probability density distributions should be used in place of single values as adopted in our description. The analysis for this case becomes similar to the approach described by Vermeulen & Cohen (1994). However, the small size and obvious incompleteness of our sample force us to use single values of the model parameters.

Under the assumptions outlined above, we obtain the probability distribution of brightness temperatures

$$p(T_{\rm b}) \propto \left[\frac{2\gamma_{\rm j}(T_0/T_{\rm b})^{\epsilon} - (T_0/T_{\rm b})^{2\epsilon} - 1}{\gamma_{\rm j}^2 - 1}\right]^{1/2} . \qquad (2)$$

Since the observed sample is biased by Doppler boosting, the lower end of the observed distribution of brightness temperatures depends on the sensitivity of VLBI data. To account for this, we use an estimate of the lowest brightness temperature that can be measured from our data, $T_{\rm lim} = 5 \times 10^8$K. Objects with brightness temperatures lower than $T_{\rm lim}$ would not be detected, implying that the distribution described by (2) includes

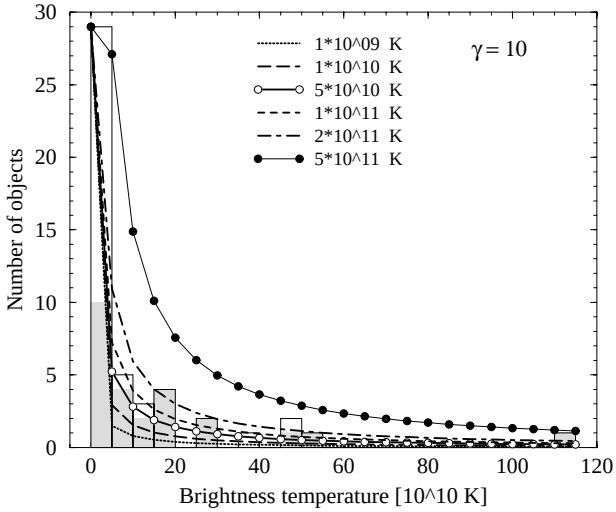

Fig. 18. Distribution of the measured brightness temperatures. The bin size is 5×10^{10}K. Shaded areas mark the VLBI cores, open areas are the jet components. Curved lines show the predicted distributions in a sample of randomly oriented jets with the given intrinsic brightness temperature, T_0. The best approximation of the observed distribution is produced by a population of jets with intrinsic brightness temperatures $T_0 \sim 0.1$–1.0×10^{11}K.

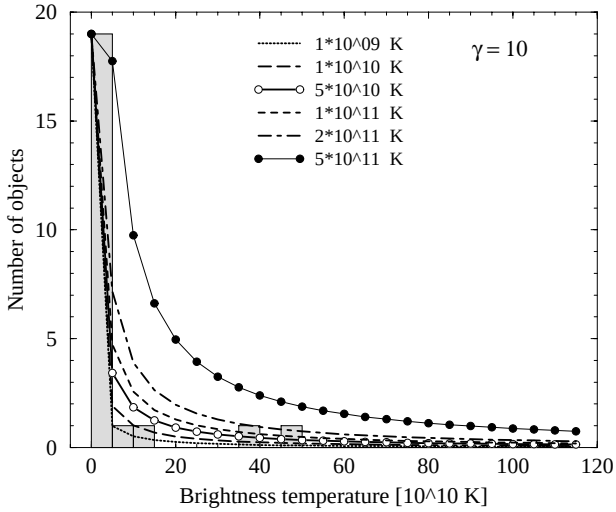

Fig. 19. Distribution of the brightness temperatures measured in the jet components. The bin size is 5×10^{10}K. Curved lines show the predicted distributions in a sample of randomly oriented jets with the given intrinsic brightness temperature, T_0. The observed distribution has most of the objects concentrated in the first bin, allowing to obtain only a crude upper limit of $T_0 \leq 5 \times 10^{10}$K.

only those sources in which the approaching jet is ejected at a viewing angle smaller than

$$\theta_{\rm lim} = \arccos\left[\frac{\gamma_{\rm j} - (T_0/T_{\rm lim})^{\epsilon}}{(\gamma_{\rm lim}^2 - 1)^{1/2}}\right]. \quad (3)$$

We normalize the results obtained from (2) to the number of objects in the lowest bin of the histogram. We choose a bin size of 5×10^{10}K and plot, in Fig. 18, a histogram of the distribution of all measured brightness temperatures (including both the cores and the jet components). For several values of T_0, the corresponding model distributions are indicated by the curves in Fig. 18. The data allow only a crude estimate of the range of intrinsic brightness temperatures which provide the best approximation of the observed distribution. We obtain $T_0 \sim 0.1$–1.0×10^{11}K. For this range of T_0, no significant intrinsic evolution of the jet emission (on the scales probed by our measurements) is needed for reproducing the observed distribution.

Fig. 18 suggests, however, that there may be a difference between the distributions of brightness temperatures measured in the cores (shaded rectangles) and in the jet components (open rectangles). For the jet components alone, our model indicates $T_0 \leq 5 \times 10^{10}$ K (Fig. 19). For the cores only, shown in Fig. 20, we obtain $T_0 \sim 1$–4×10^{11}K. For $T_0 > 5 \times 10^{11}$ K, the peak in the predicted distribution shifts rapidly toward higher brightness temperatures (for instance, the peak is found at $\sim 2 \times 10^{11}$K, for $T_0 = 10^{12}$K). Given such rapid changes of the distributions obtained with high values of T_0, we conclude that the intrinsic brightness temperature in the cores is not likely to be much higher than 5×10^{11} K.

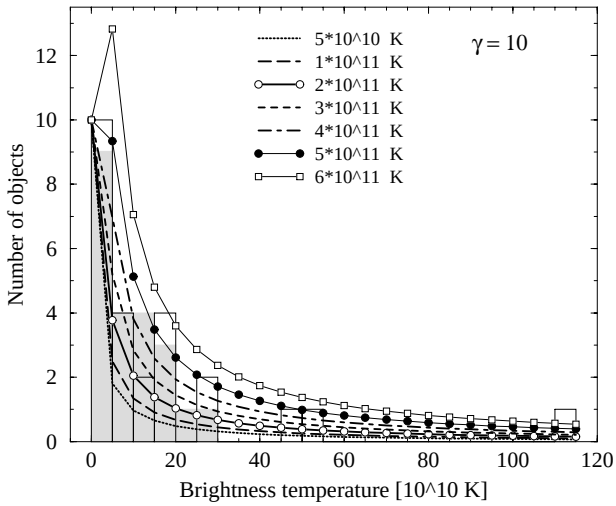

Fig. 20. Distribution of the brightness temperatures measured in the VLBI cores. The bin size is 5×10^{10}K. Curved lines show the predicted distributions in a sample of randomly oriented jets with the given intrinsic brightness temperature, T_0. Shaded areas reproduce the distribution of brightness temperatures in the same sample of objects measured with the VLBI at 15 GHz (taken from Kellermann et al. 1998). The best approximation of the observed distribution at 86 GHz is produced by a population of jets with intrinsic brightness temperatures $T_0 \sim 1$–4×10^{11}K.

4.2. Shortcomings of the population model

As we have stated above, a substantial fraction of the derived brightness temperatures may, in fact, represent only the lower limits (since many of the observed VLBI cores are likely to be unresolved). We make several comments with regard to the results obtained in the previous section:

1) The obtained model distributions cannot be made steeper, even if some of the measured $T_{\rm b}$ are only lower limits of the brightness temperature. The intrinsic brightness temperature, T_0, therefore should not be lower than the values we have derived. The T_0 may still be higher than our estimates, if most of the lower limits of the brightness temperatures are concentrated in the few lower bins of the observed distribution. In that case, the true T_0 can be higher than we have derived. However, one may expect that the lower limits are distributed rather evenly over the entire range of derived brightness temperatures, based on the correlation between the derived temperatures and measured flux densities (the χ^2-test yields a 94% probability that the two distributions are correlated; see Appendix B for the formal derivation). In this case, the derived values of the intrinsic brightness temperature T_0 should not be affected significantly by including the lower limits of brightness temperature into our data.

2) We expect that the incompleteness of our sample is the largest factor contributing to the uncertainties of the derived T_0. For a population of sources which have the same $\gamma_{\rm j}$ and T_0, one can estimate the size of a complete sample to be

$$N_{\rm tot} = \frac{n_1(\gamma_{\rm j}^2-1)}{T_1^{\epsilon}-T_{\rm lim}^{\epsilon}}\left[\frac{T_{\rm lim}T_1}{T_0}\right]^{\epsilon}\ , \qquad (4)$$

where n_1 and T_1 are the number of objects and the upper boundary of the brightness temperature in the first bin of the distribution. In our data for the cores, $n_1 = 10$, and $N_{\rm tot} \sim 100$, for $\gamma_{\rm j} = 10$. Since, for our model, $N_{\rm tot} \propto \gamma_{\rm j}^2 T_0^{1/2.7}$, the assumption made about $\gamma_{\rm j}$ affects strongly the predicted total number of sources in a complete sample. For $\gamma_{\rm j} = 5$, $N_{\rm tot} \sim 25$, which implies that the observed sample is a complete one. For higher $\gamma_{\rm j}$, the number of observed objects must be increased by a significant factor, in order to obtain a complete sample. We need a bigger sample to be able to give more definite statements on the plausibility of our scenario with a uniform intrinsic brightness temperature in compact jets. We therefore will for now view such a scenario only as an example of possible application of the measured brightness temperatures to studies of the physics of compact extragalactic jets. We shall now discuss several implications of such a scenario, not insisting anywhere in the course of the arguments that our data are sufficient for ruling out the more likely possibility of wider distribution of intrinsic brightness temperatures in compact jets.

4.3. Evolution of brightness temperature in the jets

As shown in Sect. 4.1, the T_0 indicated by our population model differs significantly (by a factor of 2–10) between the VLBI cores and the jet components. It is perhaps rather fortuitous that the VLBI cores have their derived T_0 close to the inverse-Compton limit ($\sim 5\times10^{11}$K, Kellermann & Pauliny-Toth 1969), while the T_0 derived for the jet components is consistent with the equipartition limit ($\sim 5\times10^{10}$K, Readhead 1994) for the brightness temperature. Whether or not the core and jet's T_0's are related to equipartition and Compton loss limits, the difference of the T_0 derived implies

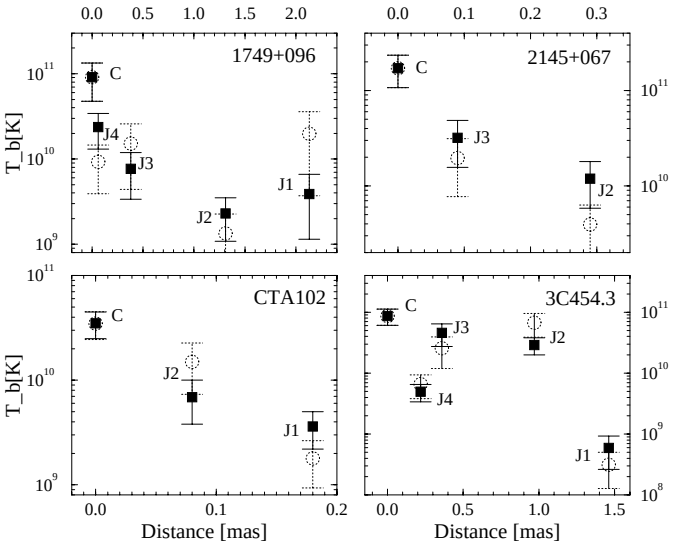

Fig. 21. Changes of the brightness temperature along the jets of several sources. Filled squares are the measured values. Open circles are the predicted brightness temperatures in shocks with adiabatic losses dominating the radio emission. The initial brightness temperature in each jet is assumed to be equal to that measured in the VLBI core of that jet.

that the jet emission should evolve substantially already on the sub-milliarcsecond scales probed by our observations. We investigate below a very basic evolutionary scheme in which the changes observed in the jet emission are caused by adiabatic energy losses in relativistic shocks.

We postulate that each of the jet components is an independent relativistic shock with adiabatic energy losses dominating the emission (see Marscher 1990). The jet plasma has a power law energy distribution $N(E){\rm d}\,E \propto E^{-s}{\rm d}\,E$, and the magnetic field is approximated as $B \propto d^{-a}$, where d is the transverse dimension of the jet (for which we will take the measured sizes of the jet components). The Doppler factor is assumed to be changing weakly throughout the jet. In this description, the brightness temperature, $T_{\rm b,J}$, of each jet component can be related to the brightness temperature of the core, $T_{\rm b,C}$, through the following proportionality:

$$T_{\rm b,J} = T_{\rm b,C}\,(d_{\rm J}/d_{\rm C})^{-\xi}\ , \qquad (5)$$

where d denotes the respective measured sizes of the core and jet feature, and $\xi = [2(2s+1)+3a(s+1)]/6$. We take the energy spectral index $s = 2.0$ (corresponding to synchrotron emission with spectral index $\alpha = -0.5$) and $a = 1$. In Fig. 21, we compare the measured brightness temperatures with the predictions by Eq. (5). The agreement between the measured and predicted $T_{\rm b}$ in the jet components is remarkable, in particular if one recalls that the predictions for all the components are obtained from a single set of model parameters. The agreement can be improved by adjusting individual spectral indices or magnetic fields of the jet components.

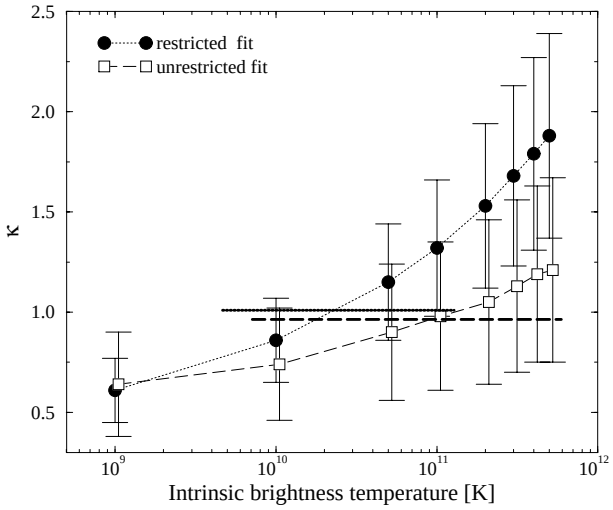

Fig. 22. Ratio, κ, between the predicted jet speeds, $\beta_{\rm pred}$, calculated from Eq. (6), and apparent speeds, $\beta_{\rm meas}$, measured from VLBI observations available in the literature. The ratio represents the slope, κ, of linear correlation $\beta_{\rm meas} \propto \kappa\beta_{\rm pred}$. The ratio is calculated for jet populations with different intrinsic brightness temperatures. The restricted fits are produced by requiring that the fits must pass through the point $(\beta_{\rm pred}, \beta_{\rm meas}) = (1, 1)$. For each type of fit, the horizontal line represents the range of acceptable T_0 for which $\beta_{\rm pred}/\beta_{\rm meas} \approx 1$.

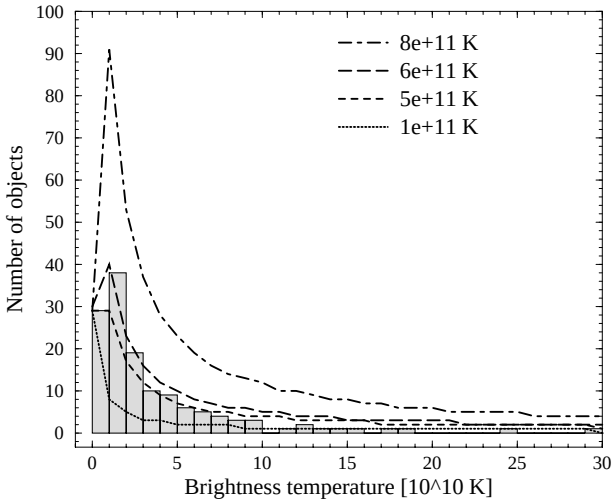

Fig. 23. Measured (rectangles; VLBI data at 15 GHz taken from Kellermann et al. 1998) and predicted (lines) distributions of brightness temperatures. The population model is the same as the one applied for the 86 GHz VLBI data presented in Figs. 15–17. The bin size is 1×10^{10}K. The limiting brightness temperature is estimated to be $\sim 10^8$K.

4.4. Brightness temperatures and jet speeds

The population model described in Sect. 4.1 can be also related to the apparent speeds in the jets. For a jet with the intrinsic brightness temperature T_0, the predicted apparent speed is:

$$\beta_{\rm pred} = \left[2\gamma_{\rm j}(T_{\rm b}/T_0)^{\epsilon} - (T_{\rm b}/T_0)^{2\epsilon} - 1\right]^{1/2} . \quad (6)$$

In Fig. 22, we compare the $\beta_{\rm pred}$ calculated for our sample with the measured speeds available from the literature. Since the enhanced emission regions in jets (for which measurements of apparent speeds are normally done) are expected to travel along curved trajectories, we use the speeds measured in the immediate vicinity of the VLBI core (determined from measurements at frequencies of 15 GHz and higher). We use averaged values for those jets which show wide ranges of observed speeds even on the scales of a few milliarcseconds. We then study a linear correlation between the measured and predicted speeds, for several values of T_0. The linear slopes determined between the predicted $\beta_{\rm pred}$ and measured $\beta_{\rm meas}$ are plotted in Fig. 22. One set of the fits is unrestricted; for the second set, we require that the fits must pass through the point ($\beta_{\rm meas}$, $\beta_{\rm pred}$) = (1,1). The latter requirement has an increasingly stronger effect at larger values of T_0. Both types of the fits imply that T_0 should not be significantly smaller than 10^{10} K. The upper limit of T_0 is not well determined by the fits, and is likely to be higher than 10^{11} K.

4.5. VLBI data at lower frequencies

Finally, we provide a brief comparison between the results obtained from our 86 GHz data and VLBI measurements of brightness temperatures at 15 GHz. We use the measurements reported by Kellermann et al. (1998) for a sample of 132 AGN. The resolution of their observations is roughly 5 times lower than in our sample, which should result in an even larger fraction of lower limits among the observed brightness temperatures. However, as we have argued earlier, the inclusion of the lower limits should not distort the picture significantly, unless the measured lower limits are found only in the lower bins of the brightness temperature distribution.

Fig. 23 shows the results of applying our population model to the data of Kellermann et al. (1998). The normalization factor (the number of sources in the first bin) is $N = 29$, in this case. The lowest value of the brightness temperature measured in the 15 GHz data is estimated to be $T_{\rm lim} = 10^8$K. With this estimate, the expected size of a complete sample is $N_{\rm tot} \sim 130$ (for $\gamma_{\rm j} = 10$). This implies that the 15 GHz data are likely to constitute a complete sample. As one can see from Fig. 23, the range of T_0 providing a satisfactory representation of the observed distribution is significantly narrower, as compared to the results obtained from our sample at 86 GHz (see Figs. 18–20). The model distributions shown in Fig. 23 imply that the best fit value of T_0 should be between 5×10^{11} K and 6×10^{11} K. To quantify this statement, we study the distribution of the χ^2-parameter of the fit for a range of T_0 and N. The results are plotted in Fig. 24. One can see immediately that all plotted χ^2-curves have a very distinct minimum, and that curves with $N = 29, 30$ give the lowest values of χ^2, with the corresponding best fit intrinsic brightness temperature $T_0 = (5.3 \pm 0.6) \times 10^{11}$ K (where the uncertainty given is the 1σ-deviation estimated from the χ^2). This value is in good agreement with the upper limit of 4×10^{11} K inferred from the data at 86 GHz. On the other hand, if the difference between the T_0 determined at 15 and 86 GHz is real, this may have serious implications about both VLBI observations at sub-millimeter wavelengths and physics of the

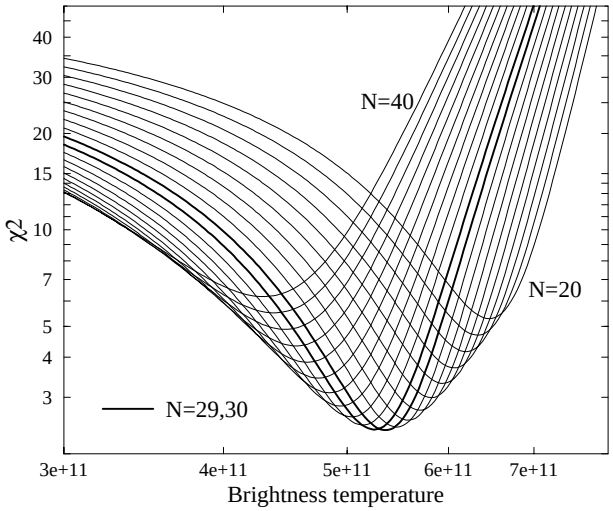

Fig. 24. Goodness of fit parameters for different population models applied to the 15 GHz data from Kellermann et al. (1998). Different curves correspond to different values of the normalization factor, N. The best fit is achieved with $N = 29$–30 and $T_0 = 5.3 \times 10^{11}$ K.

jets. If T_0 starts to decrease at 86 GHz, there will be only a few sources suitable for VLBI at 215 GHz and higher frequencies. Such a decrease of T_0 will also provide a strong argument in favor of the decelerating jet model or particle-cascade models as discussed by Marscher (1995). In view of these arguments, it is particularly important to undertake a dedicated 86 GHz VLBI study of a larger sample of extragalactic radio sources.

5. Summary

The 86 GHz VLBI survey presented here provides a significant amount of new information about the most compact regions of parsec-scale jets. For the 26 compact radio sources detected in the survey data, we have measured correlated flux densities, obtained Gaussian component modelfits, and estimated brightness temperatures in the VLBI cores and closest jet components. The observations have allowed to study the properties of compact radio emission at a 50-microarcsecond resolution in individual objects as well as for the entire sample of sources. We have shown that the changes of brightness temperature observed in the jets of several sources (1749+096, 2145+067, CTA102, and 3C454.3) are consistent with relativistic shocks in which the emission is dominated by adiabatic energy losses. We have modelled the observed distribution of brightness temperatures at 86 GHz by a population of jets moving at the same intrinsic speed and oriented randomly in the space. The model allows to estimate the intrinsic brightness temperature, T_0, in the moving jet components as $T_0 \leq 5 \times 10^{10}$K, and it gives $T_0 \sim$ 1–4 $\times 10^{11}$K for the VLBI cores. These values are close to the equipartition limit ($\sim 5 \times 10^{10}$K, Readhead 1994) and inverse-Compton limit ($\sim 5 \times 10^{11}$K, Pauliny-Toth & Kellermann 1969), respectively. The same analysis applied to brightness temperatures measured in a larger database of 132 objects observed with VLBI at 15 GHz (Kellermann et al. 1998) improves the estimate of intrinsic brightness temperature of the VLBI cores. The 15 GHz data yield $T_0 = (5.3 \pm 0.6) \times 10^{11}$K for the VLBI cores, which is basically coincident with the inverse-Compton limit. We stress that this method should be further explored by considering larger samples of sources observed with VLBI at several frequencies, and in particular by combining the brightness temperature and apparent speed measurements in those samples. With such improved databases, one may hope to be able to test more complex population models in which the intrinsic brightness temperatures and Lorentz factors in the jets are distributed over a range of values. With improved population models, it should be ultimately possible to distinguish between the accelerating and decelerating jet models.

Acknowledgements. We would like to thank K. Standke and C. Schalinski for their valuable contributions to early stages of post-processing the data. We are grateful to A.E.E. Rogers, R.S. Booth, R. Predmore, and the staff of the observatories at Effelsberg, Haystack, Pico Veleta, Quabbin, and Onsala which have participated in the observations. We thank Mark Reid and the second referee of the paper for their comments and suggestions for improving the manuscript. The Haystack Observatory is operated by the Massachusetts Institute of Technology, with support from the National Science Foundation (NSF), NASA, and the United States Air Force (USAF). The Five College Radio Astronomy Observatory is operated with support of the NSF and with permission of the Metropolitan District Commission of the Commonwealth of Massachusetts. The Onsala Space Observatory is the Swedish National Facility for Radoastronomy operated by Chalmers University of Technology. This research has made use of the Astrophysics Data System (ADS) Abstract Service and of the NASA/IPAC Extragalactic Database (NED) which is operated by the Jet Propulsion Laboratory, California Institute of Technology, under contract with the National Aeronautics and Space Administration (NASA).

Appendix A: brightness temperature distribution

The population of sources with observed brightness temperatures $T_{\rm b}$ has the same intrinsic brightness temperature, T_0, the same spectral index, α, and the same bulk Lorentz factor, $\gamma_{\rm j}$, with the corresponding jet speed $\beta_{\rm j} = (1-\gamma_{\rm j}^{-2})^{1/2}$. The sources are observed at random viewing angles, θ, and the observed distribution of $T_{\rm b}$ is determined by the distribution of Doppler factors $\delta = [\gamma_{\rm j}(1-\beta_{\rm j}\cos\theta)]^{-1}$. In this case, Eq. (1) relates the Doppler factor to the observed and intrinsic brightness temperatures. The corresponding viewing angle for a source with observed brightness temperature $T_{\rm b}$ is then found from

$$\cos\theta = (\gamma_{\rm j}^2 - 1)^{-1/2}[\gamma_{\rm j} - \delta^{-1}]^{\epsilon} \quad \text{(A.1)}$$

and

$$\sin\theta = (\gamma_{\rm j}^2 - 1)^{-1/2}[2\gamma_{\rm j}\delta^{-1} - \delta^{-2} - 1]^{1/2}\,. \quad \text{(A.2)}$$

We assume that only approaching jets are observed. For a sample without Doppler boosting bias, this implies $0 \leq \theta \leq \pi/2$, and the corresponding observed brightness temperatures ranging from

$$T_{\rm low} = T|_{\theta=\pi/2} = T_0\gamma_{\rm j}^{2-\alpha} \quad \text{(A.3)}$$

to

$$T_{\rm high} = T|_{\theta=0} = T_0[\gamma_{\rm j} - (\gamma_{\rm j}^2 - 1)^{1/2}]^{2-\alpha}\,. \quad \text{(A.4)}$$

If the sample is biased by Doppler boosting, then $T_{\rm low}$ should be substituted by the lowest brightness temperature, $T_{\rm lim}$, that can be measured from observations ($T_{\rm lim} > T_{\rm low}$ in biased samples and $T_{\rm lim} \le T_{\rm low}$ in unbiased samples). Eq. (3) gives the largest possible viewing angle, $\theta_{\rm lim}$, for the sources from the biased sample. A valid distribution can therefore be derived for all $T_0 \ge T_{\rm lim}\beta_{\rm j}^{\alpha-2}$. The probability density of the brightness temperature distribution is then $p(T_{\rm b}){\rm d}\theta = \sin\theta{\rm d}\theta$, and the probability $P(T_1 \le T_{\rm b} \le T_2)$ is given by

$$P(T_1,T_2) = 2\pi\eta_{\rm T}\int_{\theta(T_2)}^{\theta(T_1)}\sin\theta{\rm d}\theta\,, \tag{A.5}$$

where the normalization factor

$$\eta_{\rm T} = (2\pi\int_0^{\theta_{\rm lim}}\sin\theta{\rm d}\theta)^{-1} = \frac{1}{2\pi(1-\cos\theta_{\rm lim})} \tag{A.6}$$

is determined from the condition $P(0,\theta_{\rm lim}) = 1$. For a complete sample consisting of $N_{\rm tot}$ objects, the source density, $\rho = \eta_{\rm T}N_{\rm tot}$, should be used for normalization. From Eqs. (A.1) and (A.6),

$$\rho = \frac{N_{\rm tot}(\gamma_{\rm j}^2-1)^{1/2}}{2\pi[(\gamma_{\rm j}^2-1)^{1/2}-\gamma_{\rm j}+(T_0/T_{\rm lim})^{\epsilon}]}\,. \tag{A.7}$$

Then, the number of objects in a bin $[T_1,T_2]$ is given by

$$N(T_1,T_2) = N_{\rm tot}P(T_1,T_2) = \rho\int_{\theta(T_2)}^{\theta(T_1)}\sin\theta{\rm d}\theta\,. \tag{A.8}$$

For an incomplete sample, $N_{\rm tot}$ is unknown, and the normalization factor has to be determined from the number of objects in the first bin of the observed distribution. The total number of sources required for the sample to become complete can be estimated, in this case, using Eq. (4).

Appendix B: the $N(S)$-$N(T_{\rm b})$ correlation

If the measured sizes are distributed over a range of values $d_1 \le d_{\rm meas} \le d_2$, it is not necessarily true that the distributions $N(S)$ and $N(T_{\rm b})$ have to be correlated. The degree of correlation between these two distributions will depend on the formal variance $\sigma_{\rm d}^2$ of the measured sizes. Since we also include objects with upper limit estimates for the size, the lower boundary (d_1) of the distribution of measured sizes is unknown. As a result, the $N(S)$-$N(T_{\rm b})$ correlation must also depend on the binned distribution of the objects with upper limit size estimates.

Let us denote $N_{\rm t}$ – the total number of objects in the sample; $N_{\rm b}$ – the number of bins used for calculating the distributions in question; $\sigma_{\rm d}$ – variance of the measured sizes (given as a fraction of the mean measured size); κ_i – in the i-th bin: a fraction of objects with an upper limit estimate of the size. The distribution of the upper limits can be described by its mean

$$\hat\kappa = \frac{1}{N_{\rm b}}\sum_{i=1}^{N_{\rm b}}\kappa_i \tag{B.1}$$

and variance

$$\sigma_\kappa = \frac{1}{N_{\rm b}-1}\sum_{i=1}^{N_{\rm b}}(\kappa_i-\hat\kappa)^2\,. \tag{B.2}$$

Our statement that $N(S)$ and $N(T_{\rm b})$ are correlated with a probability of 94% implies that:

$$\Gamma\left(\frac{N_{\rm b}}{2},\frac{\chi^2}{2}\right) = 0.94\,, \tag{B.3}$$

where Γ is the truncated Gamma-function of order of $N_b/2$, and χ^2 is given by

$$\chi^2 = \sum_{i=1}^{N_{\rm b}}\frac{[N_i(S)-N_i(T_{\rm b})]^2}{N_i(S)+N_i(T_{\rm b})}\,. \tag{B.4}$$

For our case, we can denote $\hat\sigma^2 = \sigma_{\rm d}^2+\sigma_\kappa^2$, and give the following estimate:

$$\chi^2 \approx N_{\rm t}\frac{(\hat\sigma^2-1)^2}{\hat\sigma^2(\hat\sigma^2+1)}\,. \tag{B.5}$$

With this estimate, we obtain, from Eq. (B.3), $\hat\sigma = 0.523$. Then, using the measured $\sigma_{\rm d} = 0.468$, we get $\sigma_\kappa = 0.234$. This implies that the measured 94% probability of $N(S)$ and $N(T_b)$ to be correlated requires that the fraction of the upper limit measurements does not vary by more than 23% from one bin to another.

Appendix C: visibility distributions

In this Appendix, we present auxiliary information about several objects in the survey in which complex structures have been detected. The appendix is available only in electronic form via http://link.springer.de/link/service/journals/00230/tocs/t0364002/. Figs. 25–30 show the *uv*-sampling and visibility distributions of the 86 GHz data for 5 objects in which complex structures are implied by both model fitting and imaging. The 5 objects are: NRAO530, 1749+096, CTA102, and 3C454.3. For each object, the observed radial distribution of the visibility amplitudes is shown in the main panel, and the corresponding *uv*-plane sampling of the datapoints is given in the inset. For 2145+067, we also show a plot of visibility amplitudes and phases projected onto P.A.$= 110^\circ$, to illustrate the reliability of the structures detected in the image of this object (see Fig. 14).

References

Alberdi, A., Krichbaum T.P., Graham D., et al., 1997, A&A 327, 513
Alef W., 1989, In: Felli M., Spencer R.E. (eds.) NATO ASI Series C, vol. 283, Very Long Baseline Interferometry, Techniques and Applications. Kluwer, Dordrecht, p. 261
Airapetyan E.A., Matveenko L.I., 1997, Astronomy Letters 23, 1, 64
Beasley A.J., Dhawan V., Doeleman S.S., Phillips R.B., 1996, In: Barvainis R., Phillips R.B. (eds.) MM-VLBI Science Workshop. Haystack Observatory, Cambridge, p. 53
Blandford R.D., Königl A., 1979, ApJ 232, 34

Bondi M., Padrielli L., Fanti R., et al., 1996, A&A 308, 415
Bower G.C., Backer D.C., Wright M., et al., 1997, ApJ 484, 118
Bower G.C., Backer D.C., 1998, ApJ 507, L117
Clark B.G., 1980, A&A 89, 377
Cornwell T.J., 1995, In: Zensus J.A., Diamond P., Napier P. (eds.) Very Long Baseline Interferometry and the VLBA. CUP, Cambridge, p. 217
Doeleman S.S., 1995, Ph.D. Thesis, MIT
Doeleman S.S., Claussen M., 1996, In: Barvainis R., Phillips R.B. (eds.) MM-VLBI Science Workshop. Haystack Observatory, Cambridge, p. 37
Doeleman S.S., Bower G.C., Baker D.C., Wright M., Rogers A.E.E., 1998, In: Falcke H., Cotera A., Huschl W., Melia F., Rieke M. (eds.) The Central Parsecs, Galactic Center Workshop. ASP, San Francisco, in press
Gabuzda D.C., Cawthorne T.V., 1996, MNRAS 283, 759
Gabuzda D.C., Sitko M.L., Smith P.S., 1996, AJ 112, 1877
Kellermann K.I., Pauliny-Toth I.K.K., 1969, ApJ 155, 71
Kellermann K.I., Vermeulen R.C., Zensus J.A., Cohen M.H., 1998, AJ 115, 1295
Krichbaum T.P., Witzel A., Graham D., et al., 1992, A&A 260, 33
Krichbaum T.P., Schalinski C.J., Witzel A., et al., 1994a, In: Genzel R., Harris A.J. (eds.) The Nuclei of Normal Galaxies: Lessons from the Galactic Center. Proceedings of the NATO Advanced Research Workshop, Kluwer, Dordrecht, p. 411
Krichbaum T.P., Standke K.J., Witzel A., et al., 1994b, In: Kus A.J., Schilizzi R.T., Borkowski K.M., Gurvits L.I. (eds.) Proc. of 2nd EVN/JIVE Symposium, TRAO, Torun, p. 47
Krichbaum T.P., Britzen S., Standke K.J., et al., 1995, Proc. Natl. Acad. Sci. USA 92, 5, 11377
Krichbaum T.P., Witzel A., Graham D.A., Lobanov A.P., 1996, In: Barvainis R., Phillips R.B. (eds.) MM-VLBI Science Workshop. Haystack Observatory, Cambridge, p. 3
Krichbaum T.P., 1998, In: Falcke H., Cotera A., Huschl W., Melia F., Rieke M. (eds.) The Central Parsecs, Galactic Center Workshop. ASP, San Francisco, in press
Krichbaum T.P., Graham D.A., Witzel A., et al., 1998, A&A 335, L106
Leppänen K.J., Zensus J.A., Diamond P.J., 1995, AJ 110, 2479
Lobanov A.P., Krichbaum T.P., Witzel A., et al., 1998, A&A 340, L60
Lobanov A.P., Zensus J.A., 1999, ApJ 521, 509
Lonsdale C.J., Doeleman S.S., Phillips R.B., 1998, AJ 116, 8
Marscher A.P., 1990, In: Zensus J.A., Pearson T.J. (eds.) Parsec-scale Radio Jets. CUP, Cambridge, p. 236
Marscher A.P., 1995, Proc. Natl. Acad. Sci USA 92, 5, 11439
Marscher A.P., Broderick J.J., 1981, ApJ 249, 406
Newell S.J., Garrett M.A., Spencer R.E., 1998, MNRAS 293 L17
Otterbein K., Krichbaum T.P., Kraus A., et al., 1998, A&A 334, 489
Pearson T.J., 1991, BAAS 23, 991
Rantakyrö F.T., Bååth L.B., Dallacasa D., Jones D.L., Wehrle A.E., 1996, A&A 310, 66
Rantakyrö F.T., Bååth L.B., Backer D.C., et al., 1998, A&AS 131, 451
Readhead A.C.S., 1994, ApJ 426, 51
Reuter H.-P., Kramer C., Sievers A., et al., 1997, A&AS 122, 271
Rogers A.E.E., Cappallo R.J., Hintegger H.F., et al., 1983, Sci 219, 51
Rogers A.E.E., Doeleman S.S., Wright M.C., et al., 1994, ApJ 434, L59
Rogers A.E.E., Doeleman S.S., Moran J.M., 1995, AJ 109, 1391
Ros E., Zensus J.A., Lobanov A.P., 1999, New Astronomy Reviews 43, 717
Schalinski C.J., Witzel A., Krichbaum T.P., et al., 1994, In: Zensus J.A., Kellermann K.I. (eds.) Compact Extragalactic Radio Sources. NRAO, Green Bank, p. 45
Shepherd M.C., Pearson T.J., Taylor G.B., 1994, BAAS 26, 987
Standke K.A., Graham D.A., Krichbaum T.P., et al., 1994, In: Sassao T., Manabe S., Kameya O., & Inoue M. (eds.) VLBI Technology, Progress and Future Observational Possibilities. Terra, Tokyo, p. 75
Vermeulen R.C., Cohen M.H., 1994, ApJ 430, 467
von Linde J., Borgeest U., Schraml K.-J., et al., 1993, A&A 367, L23